Diffusion, Thermal Properties and Chemical Compatibilities of Select MAX Phases with Materials For Advanced Nuclear Systems

Nuclear Energy Enabling Technologies

Michel W. Barsoum

Drexel University

In collaboration with:

Savannah River National Laboratory

NEUP | Nuclear Energy University Programs

U.S. Department of Energy

NEUP Final Report 2015

Project Title: Diffusion, Thermal Properties and Chemical Compatibilities of Select MAX Phases with Materials For Advanced Nuclear Systems
Project Number: CFP-11-3231
University Principal Investigator: Michel W. Barsoum (Drexel University)
Collaborators: Grady Bentzel and Darin J. Tallman (Drexel University), Brenda Garcia-Diaz, Elizabeth Hoffman and Robert Sindelar (Savannah River National Lab, Aiken SC)

Project Description:

The demands of Gen IV nuclear power plants for long service life under neutron irradiation at high temperature are severe. Advanced materials that would withstand high temperatures (up to 1000+ ºC) to high doses in a neutron field would be ideal for reactor internal structures and would add to the long service life and reliability of the reactors. The objective of this work is to investigate the chemical compatibility of select MAX with potential materials that are important for nuclear energy, as well as, to measure the thermal transport properties as a function of neutron irradiation. The chemical counterparts chosen for this work are: pyrolytic carbon, SiC, U, Pd, FLiBe, Pb-Bi and Na; the latter 3 in the molten state. The thermal conductivities and heat capacities of non-irradiated MAX phases will be measured.

Accomplishments for FY2015 Q4:

Task A: Diffusion Bonding of Zircaloy-4 and Select MAX phases

Our paper entitled "Reactivity of Zircaloy with Ti_3SiC_2 and Ti_2AlC in the 1100 to 1300 °C Range" has been published in the *J. Nucl. Mater.*, **460**, pp. 122-129 (2015).

Task B: Diffusion bonding with SiC and Pyrolytic Graphite, PG

Our paper entitled "On the Interactions of Ti_2AlC, Ti_3AlC_2, Ti_3SiC_2 and Cr_2AlC with Silicon Carbide and Pyrolytic Carbon at 1300 °C" has been published in the *J. of the European Ceramic Society*, **35**, pp 4107-4114 (2015).

Task B: Reactions with Palladium

A paper entitled "On the interactions of Ti_2AlC, Ti_3AlC_2, Ti_3SiC_2, and Cr_2AlC with Palladium at 900 °C", is in the final stages of the drafting process and will soon be submitted for publication to J. Amer. Cer. Soc.

Task C: Reaction with Molten Metals

A paper titled "On the Interactions of Ti_2AlC, Ti_3AlC_2, Ti_3SiC_2 and Cr_2AlC with pure Sodium at 550 °C and 750 °C", has been submitted to *Corrosion Science*. The first stage of the review process has been completed, and the revised paper, with a rebuttal to reviewer comments, has been re-submitted for publication.

Task D: Thermal Diffusivity and Conductivity

A paper is currently being drafted on this work and will be submitted to *Scripta Materialia*.

Task E: He Permeation

A paper entitled, "*Helium Permeability of the Ti$_2$AlC, Ti$_3$AlC$_2$, and Ti$_3$SiC$_2$ MAX Phases at 850 °C and 950 °C*", is in the final stages of the drafting process, and should soon be submitted for publication in J. of Nuclear Materials.

Table of Contents:

List of Figures:

All Figures are located in Appendix A.

Figure 12: XRD patterns of the interface between , a) Ti$_2$AlC, b) Ti$_3$AlC$_2$, c) Ti$_3$SiC$_2$, and d) Cr$_2$AlC, with, I), Pd after heating at 900 °C for 2 h, and, II), control.

Figure 13: a) Backscatter electron SEM micrographs of the Ti$_2$AlC/Pd interface after heating to 900 °C 10 h, with elemental mappings of, b) Al, c) Pd, and, d) Ti.

Figure 14: a) Backscatter electron SEM micrographs of the Ti$_3$AlC$_2$/Pd interface after heating to 900 °C 10 h, with elemental mappings of, b) Al, c) Pd, and, d) Ti.

Figure 15: a) Backscatter electron SEM micrographs of the Ti$_3$SiC$_2$/Pd interface after heating to 900 °C 10 h, with elemental mappings of, b) Si, c) Pd, and, d) Ti.

Figure 16: a) Backscatter electron SEM micrographs of the Cr$_2$AlC/Pd interface after heating to 900 °C 10 h, with elemental mappings of, b) Al, c) Pd, and, d) Cr.

Figure 17: a) HRTEM, and diffraction patterns in the, b) [1121] and, c) [1120] directions of the (Ti,Pd)$_3$SiC$_2$ area from the Ti$_3$SiC$_2$/Pd 900 °C for 2 h sample.

Figure 18: Bulk XRD patterns of surfaces exposed to Na at 750 °C for 168 h of, a) Ti$_2$AlC, b) Ti$_3$AlC$_2$, c) Ti$_3$SiC$_2$, and d) Cr$_2$AlC. Red squares represent the MAX peaks; blue circles represent binary carbide peaks. The latter were the major impurities found in the as-fabricated samples.

Figure 19: Micrographs of Ti$_3$SiC$_2$, a) reacted and etched surface, OM; b) unreacted, SE SEM; c) reacted, SE SEM; d) reacted, BS SEM, and Cr$_2$AlC, e) reacted and etched surface, OM; f) unreacted, SE SEM; g) reacted, SE SEM; and, h) reacted, BS SEM, respectively, after contact with Na at 750 °C for 168 h.

Figure 20: Micrographs of Ti$_2$AlC, a) reacted and etched surface, OM; b) unreacted, SE SEM; c) reacted, SE SEM; d) reacted, BS SEM, and Ti$_3$AlC$_2$ a) reacted and etched surface, OM; b) unreacted, SE SEM; c) reacted, SE SEM; and, d) reacted, BS SEM, respectively, after contact with Na at 750 °C for 168 h.

Figure 21: TEM micrographs of Ti$_3$AlC$_2$ after contact with Na at 750 °C for 168 h, a) with objective aperture, and, b), normal bright field. Diffraction patterns for grains 1 and 2 are shown as insets.

Figure 22: Thermal conductivities of various MAX phases as a function of temperature.

Figure 23: Permeability coefficient k' of Ti$_2$AlC, Ti$_3$AlC$_2$ and Ti$_3$SiC$_2$ at 850°C and 950°C.

List of Tables:

All Tables are located in Appendix B.

Summary Task A: Diffusion Bonding of Zircaloy-4 and Select MAX phases

Zircaloy-4 (Zr-4) is widely used as fuel cladding in light water reactors (LWR), mainly due to its high strength, corrosion resistance and low neutron cross section. However, its poor oxidation resistance can lead to its failure under loss of coolant conditions.[1-3] Up to 850 °C, α-zirconium (α-Zr) maintains an HCP structure. Above 950 °C, a phase change occurs resulting in FCC β-zirconium (β-Zr).[4] LWRs nominally operate up to 400 °C, well within the α-Zr region for Zr-4.[5] Loss-of-coolant accidents (LOCA), however, can lead to fuel rods experiencing temperatures in excess of 1200 °C, their rupture due to increased pressure, and exposure to the atmosphere with catastrophic consequences.[4]

Another issue with Zr-4 cladding is its susceptibility to water corrosion, specifically hydrogen pickup and embrittlement.[5] Dissolved oxygen in the coolant water reacts with the metal surface, leading to the formation of a protective layer of ZrO_2. Simultaneously, the hydrogen produced from the oxidation diffuses into the cladding, resulting in the generation of zirconium hydride, ZrH_2, precipitates, which lead to hydrogen embrittlement, decreases in fracture toughness and the acceleration of corrosion and irradiation swelling.[5] Mitigation of hydrogen pickup and cladding oxidation is thus vital for the longevity and accident tolerance of fuel rod assemblies for use in LWRs. As important, isolating the Zr-cladding during normal operating conditions could allow for higher burn-up and possibly higher operating temperatures. One solution to the corrosion problem, that could also increase the safety of a LWR in LOCA, is to hermetically seal them from their surroundings. We recently proposed that the MAX phases in general, and Ti_2AlC in particular, can be used to as a thin coating onto existing Zr-4 cladding.[6]

The reactivity between Zr-4 and Ti_3SiC_2 and Ti_2AlC, over the 1100-1300 °C temperature range, was studied by setting up TSC/Zr-4 and TAC/Zr-4 diffusion couples. Based on the results shown, and similar to previous work in the Zr/Al system, it is clear that Al-diffusion into Zr was extensive, and resulted in a large affected diffusion zone with several Zr_xAl_y intermetallic layers.[7-9] Zr_3Al precipitates were observed up to 200 μm into the Zr-4 bulk after annealing at all conditions. The Al diffused out of the TAC basal planes and through the grain boundaries, resulting in the formation of TiC rings around TAC grains near the bonding interface.

Diffusion of Si from TSC generally formed two intermetallic layers: ZrSi and Zr_3Si. At higher temperatures, layers of $ZrSi_2$, Zr_3Si_2, and Zr_2Si also formed. In this case, TiC layers were not seen to form around any of the TSC grains.

Overall, diffusion depths from Ti_3SiC_2 were an order of magnitude shallower than the Al-containing MAX phases at 1100 and 1200 °C, and 5-7 times shallower at 1300 °C. The diffusion of both Si and Al is seen to follow the parabolic law, and the microstructure of the diffusion bonded regions is indicative of the diffusion controlled reaction.

Summary Task B: Diffusion bonding with SiC and Pyrolytic Graphite, PG

Currently, there is limited research in the open literature on the chemical stability of the MAX phases vis-à-vis materials for nuclear systems. Certain MAX phases have been tested for corrosion in select coolant environments. For example, it has been shown that Ti_3SiC_2 has superb corrosion resistance to molten Pb and Pb-Bi alloys.[10,11] The diffusion between Zircaloy-4 and the MAX phases Ti_3SiC_2 and Ti_2AlC in the 1100-1300 °C range has also been explored.[12] These results show the A-group element diffusing out of the MAX phase and forming intermetallics with the Zr-4, with the penetration depth of the Si in Ti_3SiC_2 being roughly an order of magnitude less than that of the Al from the Ti_2AlC.

Silicon carbide, SiC, and pyrolytic graphite, PG, are used as diffusion barrier layers in the TRISO fuel design.[13] A MAX phase layer may prove to be useful in extending the lifetime of TRISO fuel pellets. They could be used either as an additional layer that maintains thermal diffusion efficiency, or as a substitute to the current SiC layer. Furthermore, because Ti_2AlC and Ti_3AlC_2 form thin alumina protective layers when heated in air they have been shown to have excellent oxidation resistance at temperature up of 1400 °C, even under severe cyclic heating conditions.[14] The same compounds are also stable in high vacuum, to temperature up to 1400 °C.[15] At 1000 and 1100 °C, Cr_2AlC also forms a thin alumina layer, but with a thin Cr_7C_3 underlayer.[16] At 1200 and 1300 °C, an outer $(Al_{1-x},Cr_x)_2O_3$ mixed oxide layer, an intermediate Cr_2O_3 oxide layer, an inner Al_2O_3 oxide layer, and a Cr_7C_3 underlayer form. At these temperatures, spallation occurs, limiting oxidation resistance of Cr_2AlC to no higher than 1100 °C, or even 1000 °C.[17]

At 1300 °C and for times as long as 30 h under a load corresponding to a stress of about 30 MPa, neither Ti_3SiC_2 nor Cr_2AlC (Figs. 6 and 7, respectively) showed any evidence of a reaction with SiC. The 10 μm thick layer of TiC formed on Ti_2AlC (Fig. 8) was thinner than the corresponding layer formed when Ti_2AlC was heated in the vacuum of the hot press. Said otherwise, the presence of SiC must have slowed down the escape of the Al from the Ti_2AlC phase. The TiC layer that formed on Ti_3AlC_2 (Fig. 9), on the other hand, was roughly double the ~15 μm thick layer that formed in the vacuum of the hot press.

No evidence for a reaction was found between Ti_3SiC_2 or Ti_2AlC (above that in vacuum) with PG (Figs. 6 and 8, respectively). In the case of Cr_2AlC (Fig. 7), neither OM or SEM micrographs show much evidence for a reaction. However, XRD unambiguously showed that

Cr_7C_3 and Cr_3C_2 formed at the interface with the PG (Fig. 10). In the case of Ti_3AlC_2 (Fig. 9), the TiC layer was about 100 µm thick.

Summary Task C: Reactions with Palladium

Certain MAX phases have been tested for corrosion in select coolant environments. For example, it has been shown that Ti_3SiC_2 has superb corrosion resistance to molten Pb and Pb-Bi alloys.[10,11] Fission products, such as tritium and palladium, Pd, must also be considered. SiC and pyrolytic C are used as diffusion barrier layers in the TRISO fuel design,[13] however, SiC has been shown to be susceptible to Pd attack.[18-21] As Pd evolves from the fuel, it becomes a major factor in SiC corrosion, leading to cladding failure. It has been reported[20,21] that Pd nodule attack has led to a thinning of the SiC locally. A complete penetration of Pd through the SiC layer presents an open path for other fission product transport, leading to a functional failure of the SiC.[20] Other binary carbides and nitrides have been tested to compare their resistance to Pd versus SiC.[22,23] Tan et al.[22] found that all four of the binary carbides tested showed better resistance to Pd attack than SiC, with TiN and ZrN having the best resistance, followed by TiC and ZrC. After heating to 1400 °C for 10 h in a high purity Ar atmosphere, the formation of $TiPd_{(3+x)}$, $ZrPd_3$, and C were found in the TiC-Pd and ZrC-Pd diffusion couples, in their respective systems. Pd attack along the TiC grain boundaries was observed, with only a limited attack along the ZrC grain boundaries. No intermediate phases were observed in the TiN-Pd diffusion, but a small amount of $ZrPd_3$ and C was observed in the ZrN-Pd diffusion couple.[22] Demkowicz et al. also tested TiN, TiC, and SiC with Pd, up to temperatures of 1600 °C, and, again, found that both TiC and TiN have a lower reactivity with Pd than SiC. With the use of TEM, they found that the TiPd3 phase formed at the TiC-Pd interface, with a Pd/Ti ration ≤ 3and an ordered AuC_3 structure. For the TiN-Pd interface, only Pd(Ti) solid solutions with FCC structure were observed. Based on these results, it is expected that at least some of the selected MAX phases herein will show similar resistance to Pd attack. A MAX phase layer may prove to be useful in extending the lifetime of TRISO fuel pellets. They could be used either as an additional layer that maintains thermal diffusion efficiency, or as a substitute to the current SiC layer.

Herein, we focus on the interactions, at 900 °C, of Pd with Ti_2AlC, Ti_3AlC_2, Ti_3SiC_2 and Cr_2AlC. Both Ti_2AlC and Ti_3AlC_2 (Fig. 11) behaved in a similar fashion to the reaction between TiC and Pd described by Tan et al.[22] and Demkowicz et al.[23] In both cases, Pd was found to diffuse along the grain boundaries into the MAX, showing the formation of $TiPd_3$, as seen in XRD (Fig. 12) of the interfaces. Through the use of EDS (Fig. 13 and 14), a migration of Al into

the Pd was detected, suggesting the formation of palladium aluminide. Neither Ti_3SiC_2 nor Cr_2AlC (Fig. 11, and Figs. 15 and 16, respectively), however, showed any sign of this grain boundary diffusion of Pd. Ti_3SiC_2, on the other hand, behaved more like SiC,[18-21] than TiC,[22,23] showing a quite rapid diffusion of Pd into the MAX. Similar to Al in Ti_2AlC and Ti_3AlC_2, Si in Ti_3SiC_2 diffuses into Pd, leading to the formation of palladium silicide, with EDS suggesting the Pd_9Si_2 phase. Evidence also points to the likelihood that a solid solution MAX phase is formed between Ti_3SiC_2 and Pd (Fig. 17), with EDS results suggesting the $(Ti_{0.75},Pd_{0.25})_3SiC_2$ stoichiometry. After heating to 900 °C for 10 h, the diffusion layer thickness in Ti_2AlC/Pd, Ti_3AlC_2/Pd, Ti_3SiC_2/Pd, and Cr_2AlC/Pd was found to be 35 µm, 105 µm, 410 µm, and 45 µm, respectively, suggesting that the best resistance to Pd attack follows, from best to worst, Ti_2AlC, Cr_2AlC, Ti_3AlC_2, and Ti_3SiC_2.

Summary Task D: Reaction with Molten Metals

Coolants that have attracted interest for the next generation nuclear reactors includes, He gas, molten Na, Pb-Bi and FLiBe.[13,24,25] Certain MAX phases have been tested for corrosion in select coolant environments. For example, it has been shown that Ti_3SiC_2 has superb corrosion resistance vis-à-vis molten Pb and Pb-Bi alloys.[10,11] Over the last 50 years, the idea of liquid metal cooled fast reactors (LMFR) has been conceived, researched, and even implemented.[26] Due to its abundance and relative low cost compared to other coolants, liquid Na has been considered as an attractive coolant.[27] Over the years, there have been experimental Na cooled LMFRs in France (Rapsodie), Germany (KNK-II), India (FBTR), Japan (JOYO), Russia (BOR-60 and BR-10), the US (EBR-II, Fermi, and FFTF), and one currently under construction in China (CEFR). Of the commercial liquid cooled LMFRs, there was the Super-Phénix 1 in France,[26] commissioned in 1986 and decommissioned in 1997. The structural materials used in contact with molten Na have been varying stainless steels, mainly 316, and those containing higher concentrations of Cr and Ni.[26]

Studies have been conducted to observe the interaction of select stainless steels with liquid Na. One study, performed by Suzuki et al.[28] explored the reactivity of numerous stainless steel alloys, including 316SS, by flowing molten Na at a rate of 4 m/s at 700 °C and evaluating the specimens after 426, 1723, 2395 and 4066 h. They found that for all alloys, Cr and Ni were selectively dissolved. The decrease in the concentration of these elements was initially rapid, but began to level off after 2000 h, and, after 4000 h, the concentration of Cr and Ni became stable. Optical microscopy, OM, of the cross sections showed the formation of the σ-phase (a chromium/molybdenum-rich intermettalic phase)[29] to be approximately 50 μm from the surface in 316SS. All alloys tested except for a low Mo content alloy formed small, surface corrosion nodes rich in Mo and Fe. The attack by Na on some of the alloys was determined to be due to their higher Ni content, which showed signs of intergranular attack of more than 10 μm, as well as pores of less than 10 μm on the surface. Another study, conducted by Ganesan et al.[30] explored the reactivity between annealed 316 stainless steels and static Na at 773 and 873 K for durations ranging from 500 to 2000 h in an Ar atmosphere. Again, it was found that Fe-Mo corrosion resistant nodes were formed on the exposed surfaces. Ganesan et al.[30] also found the post-exposure weight losses for the annealed samples, under static Na, were less than those reported in dynamic Na environments.[31] The weight loss in the annealed samples was also seen

to be less than the 20% found in cold worked 316 stainless steel samples.[32,33] As with Suzuki et al.[28] the σ-phase was found to nucleate near the exposed surfaces. An increase in micro-hardness - from 150±7 V_H to 250±10 after exposure to Na - was also noted.[30]

The interactions between polycrystalline samples of Ti_2AlC, Ti_3AlC_2, Ti_3SiC_2 and Cr_2AlC, and pure, static Na at 550 °C and 750 °C for 168 h was studied for the first time. The MAX samples were placed in sealed stainless steel tubes. Based on a comparison of pre- and post-XRD (Fig. 18), OM, SEM (Figs. 19-20), and TEM micrographs (Fig. 21), EDS, and Vickers microhardness measurements (Table 1), we conclude that not only are the Ti_3SiC_2, Cr_2AlC and Ti_2AlC compositions relatively stable vis-à-vis exposure to molten Na, but also their grain boundaries. In contradistinction, the evidence shows that while the bulk of the Ti_3AlC_2 sample is stable, the grain boundaries are not and appear to have been attacked by the molten Na. TEM (Fig. 21) and EDS results suggest a migration of Al to the grain boundaries, and into the molten Na.

Summary Task E: Thermal Diffusivity and Conductivity

Thermal conductivity is one of the more important properties required for fuel cladding materials in nuclear reactors. In order to remove generated heat from the fuel pellets, fuel cladding must possess good thermal conductivity, and maintain it at elevated temperatures and irradiation doses. SiC has shown a significant decrease in thermal conductivity with irradiation.[34] The thermal diffusivity, α, of several non-irradiated MAX phases and solid solution MAX phases was measured as a function of temperature, and used to calculate thermal conductivity, κ_{th}.

Samples of Ti_3SiC_2-FG, Ti_3SiC_2-CG, Ti_3AlC_2, Ti_2AlC, and Ti_2AlN were sourced from leftover blanks fabricated for a previous irradiation study.[35] Solid solutions were explored in order to begin analysis of Zr-containing MAX phases for use in thermal reactor applications where low neutron cross section is desirable. Pure Zr_2AlC is not thermodynamically stable, thus solid solutions with Nb and Ti were prepared to explore the addition of Zr.

Test specimens were machined via EDM into 12.5 mm dia. × 3 mm thick discs and polished down to a final surface preparation of 3μm diamond suspension on both sides to form parallel faces. Prior to testing with the laser flash analysis technique, the surfaces of each sample were plasma coated with a 5 μm graphite layer to ensure absorption of the laser pulses.

Thermal diffusivity measurements were collected by laser flash analysis (LFA 427, Netzsch, Boston, MA) using 1 ms pulses at 500V and 0.4 hz. The temperature signal was recorded with an infrared detector directly on the rear face of the sample. Temperature measurements were collected twice every 25K from 298 to 1223 K. The tests were performed in 99.995% Ar atmosphere flowing at 100 ml/min after an initial vacuum of 10^{-3} torr.

The goal of this work was to measure the κ_{th} of several MAX phases as a function of temperature, and compare the results with extrapolated κ_{th} from resistivity results from neutron irradiation MAX phases. Notably, κ_{th} does not decrease significantly for Ti_3SiC_2, Ti_3AlC_2, Ti_2AlC or Cr_2AlC over the wide range of temperatures studied (Fig. 22). These results bode well for MAX phases to be used as fuel cladding material, as κ_{th} was maintained at high temperatures. Irradiation defects will only decrease κ_{th}, thus possessing a high baseline at elevated temperatures is promising result (Table 2). Using the Wiedmann-Franz law to correlate thermal transport with electrical resistivity, the thermal conductivity of irradiated MAX phases was estimated using previously reported electrical resistivity results (Table 3).[35] The defect

clusters that are observed at 350 °C[35] resulted in a degradation of electrical transport, which correlates to a reduction in thermal conductivity. Irradiation at higher temperatures, however, resulted in large, coherent dislocation loops, which did not have as large an impact on electrical transport.[35] From these results, it is clear that irradiation at temperatures as low at 695 °C resulted in good recovery of RT electrical conductivity for these MAX phases, and by association thermal conductivity. These results compare well with κ_{th} values of the MAX phases measured at 300K by laser flash analysis earlier in this section. The improved defect recovery that occurs in these MAX phases, notably Ti_3SiC_2, during high temperature neutron irradiation bodes well for these materials for use in high temperature neutron applications.

Summary Task F: He Permeation

In the literature, permeation is commonly reported in terms of a permeability coefficient, which is also called the permeation or permeability constant, or just permeability. In some cases, the models used to calculate the permeability are different or a variety of units are used making the comparison of the results not a straight forward task. Often, the terms permeability and permeance are confused as well. Permeability is not dependent on the thickness of the material while permeance does depend on the on the thickness of the material.

He permeability tests were performed at 850°C and 950°C for three MAX phase material samples: Ti_2AlC, Ti_3AlC_2 and Ti_3SiC_2 following a similar procedure described in the ASTM D1434.[40] Each sample was machined to a diameter of 12 mm with a thickness of 3 mm.

A customized differential pressure (DP) rig was designed by Savannah River National Laboratory (SRNL) personnel to mount the samples for the high temperatures tests. The samples were supported by a sintered disc in order to prevent mechanical failure. The DP rig has two parts that clamp into the sample, each with a stainless steel Swagelok fitting to which gas lines to the external system were connected. After clamping the edges of the samples, the area exposed is 10 mm diameter. The sample chamber was housed in a furnace that is capable of temperatures up to 1000°C. Just outside the furnace, pressure gauges were fitted; an analogue high pressure on the high pressure line, and a digital vacuum gauge on the low pressure line. A computer and control box were used to interface with the sample chamber. The lines were controlled with valves to allow either gas inlet (on the high P test gas side) or vacuum (on both sides). The pressure was regulated from a nearby cylinder with a reservoir attached to prevent the regulator from controlling the rate. The readings from the digital vacuum gauge were logged.

In the differential pressure test, both sides of the sample chamber were evacuated and then the system was isolated. The sample chamber was then allowed to stand for the test period of 2 hr and the increase in pressure in the low pressure side was regarded as the baseline. Subsequently, another evacuation was performed and He gas was supplied at 0.5 bar to the high pressure side. The pressure on the high pressure side was maintained throughout the test run at 0.5 bar, whereas the pressure on the low pressure side was allowed to rise and the rate at which this occurred was measured. A LabVIEW program was used to calculate and record permeation rate dynamically.

Herein we report on the He permeability of the Ti_2AlC, Ti_3AlC_2 and Ti_3SiC_2 MAX phases, performed at 850 °C and 950 °C. At constant temperature, the He permeability decreases for the material type as follows: $Ti_2AlC > Ti_3SiC_2 > Ti_3AlC_2$ by about an order of magnitude difference between each value. These materials showed between 15.5% and 35.3% increase in He permeability at 950 °C as compared to their respective permeabilities at 850 °C (Tables 4-6). These He permeability results are comparable to those in literature for alumina at similar temperatures (Fig. 23), and show the same order of magnitude of permeability at high temperatures as room temperature measurements in SiC/SiC composites. These results indicate a significant ability for these MAX phases to contain and limit the transport of He through bulk.

References:

1. Berger, P.; El Tahhann, R.; Moulin, G.; Viennot, M., Nuclear Instruments and Methods in Physics Research Section B: Beam Interactions with Materials and Atoms **210** (2003) 519-525.
2. Garcia, E. A.; Béranger, G., Journal of Nuclear Materials **273** (1999) 221-227.
3. Steinbrück, M.; Birchley, J.; Boldyrev, A. V.; Goryachev, A. V.; Grosse, M.; Haste, T. J.; Hózer, Z.; Kisselev, A. E.; Nalivaev, V. I.; Semishkin, V. P.; Sepold, L.; Stuckert, J.; Vér, N.; Veshchunov, M. S., Progress in Nuclear Energy **52** (2010) 19-36.
4. Alam, T.; Khan, M. K.; Pathak, M.; Ravi, K.; Singh, R.; Gupta, S. K., Nuclear Engineering and Design **241** (2011) 3658-3677.
5. Allen, T. R.; Konings, R. J. M.; Motta, A. T., 5.03 - Corrosion of Zirconium Alloys. In *Comprehensive Nuclear Materials*, Konings, R. J. M., Ed. Elsevier: Oxford, 2012; pp 49-68.
6. Tallman, D. J.; Hoffman, E. N.; Vinson, D.; Sindelar, R. L.; Kohse, G.; Barsoum, M. W. In *Effects of Neutron Irradiation on Select MAX Phases*, AIP Conference Proceedings, American Institute of Physics, Ste. 1 NO 1 Melville NY 11747-4502 United States: 2012.
7. Kidson, G. V.; Miller, G. D., Journal of Nuclear Materials **12** (1964) 61-69.
8. Yue, T. M.; Xie, H.; Lin, X.; Yang, H. O., Journal of Alloys and Compounds **509** (2011) 3705-3710.
9. Laik, A.; Bhanumurthy, K.; Kale, G. B., Journal of Nuclear Materials **305** (2002) 124-133.
10. L. A. Barnes, N. L Dietz Rago, and L. Leibowitz, *J. Nucl. Maters.*, **373**, 424-428 (2008).
11. A. Heinzel, G. Muller, and A. Weisenburger, *J. Nucl. Maters.*, **392**, 255-258 (2009).
12. D. J. Tallman, J. Yang, L. Pan, B. Anasori, and M. W. Barsoum, *J. Nuc. Mat.*, **460**, 122-129 (2015).
13. T. Allen, J. Busby, M. Meyer, and D. Petti, *Materials Today*, **13**, 14 (2010).
14. M. Sundberg, G. Malmqvist, A Magnusson, and T. El-Raghy, *Cermaics International*, **30**, 1899-1904 (2004).
15. D. Tallman, B. Anasori, and M. W. Barsoum, *Mater. Res. Lett.*, **1**, 115-125 (2013).
16. D. B. Lee and T. D Nguyen, *J. Alloys Compds.*, **464**, 434-439 (2008).
17. I. M. Low, W. K. Pang, S. J. Kennedy, and R. I Smith, *J. Eur. Ceram. Soc.*, **31**, 159-166 (2011).

18. W. Schenk, G. Pott, and H. Nabielek, *J. Nucl. Maters.*, **171**, 19-30 (1990).
19. K. Minato, T.Ogawa, K. Fukuda, M. Shimizu, Y. Tayama, and I. Takahashi, *J. Nucl. Maters.*, **208**, 266-281 (1994).
20. G.K. Miller, D.A. Petti, J.T. Maki, and D.L. Knudson, *J. Nucl. Maters.*, **355**, 150-162 (2006).
21. K. Minato, T. Ogawa, S. Kashimura, and K. Fukuda, *J. Nucl. Maters.,***172**, 184-196 (1990).
22. L. Tan, T.R. Allen, and P. Demkowicz, *Solid State Ionics*, **181**, 1156-1163 (2010).
23. P. Demkowicz, K. Wright, J. Gan, D. Petti, *Solid State Ionics*, **179**, 2313-2321 (2008).
24. J. Kemsley, *Chemical &Engineering News*, **88**, 29-31 (2010).
25. S. Delpech, C. Cabet, C. Slim, and G. S. Picard, **13**, 34 (2010).
26. A. Rineiskii, A. Stanculescu, and Y. Yanev, *Interational Atomic Energy Agency*, TECDOC-1531 (2006).
27. A. Rineiskii, W. Mandl, A. Badulescu, Y. I. Kim, A. Stanculescu, and Y. Yanev, *Interational Atomic Energy Agency*, TECDOC-1569 (2007).
28. T. Suzuki, I. Mutoh, T. Yagi, and Y. Ikenaga, *Journal of Nuclear Materials*, **139**, 97-105 (1986).
29. X. Tang, *Microscopy and Microanalysis*, **11**, 78-79 (2005).
30. V. Ganesan, and V. Ganesan, *Journal of Nuclear Materials*, **256**, 69-77 (1998).
31. H. U. Borgstedt, and J. M. Dahlke, *CONF-800401-P1*, Richland, Washington, DC, 7-11 (1980).
32. T. Suzuki, I. Mutoh, T. Yagi, and Y. Ikenaga, *Journal of Nuclear Materials*, **139**, 97-105 (1986).
33. T. Suzuki and I. Mutoh, *Journal of Nuclear Materials*, **140**, 56-62 (1986).
34. L.L. Snead, *Journal of Nuclear Materials*, 329–333, Part A (2004) 524-529.

35. Tallman, D. J.; Hoffman, E. N.; Garcia-Diaz, B. L.; Vinson, D.; Sindelar, R. L.; Kohse, G.; Barsoum, M. W., Acta Materialia **85** (2014) 132-143.
36. M.W. Barsoum, T. El-Raghy, C.J. Rawn, W.D. Porter, H. Wang, E.A. Payzant, C.R. Hubbard, *Journal of Physics and Chemistry of Solids*, **60** (1999) 429-439.
37. T. Scabarozi, A. Ganguly, J.D. Hettinger, S.E. Lofland, S. Amini, P. Finkel, T. El-Raghy, M.W. Barsoum, *Journal of Applied Physics*, **104** (2008) 073713-073713-073716.
38. M.W. Barsoum, I. Salama, T. El-Raghy, J. Golczewski, H.J. Seifert, F. Aldinger, W.D. Porter, H. Wang, *Metallurgical and Materials Transactions A*, **33** (2002) 2775-2779.
39. W. Tian, P. Wang, G. Zhang, Y. Kan, Y. Li, D. Yan, *Scripta Materialia*, **54** (2006) 841-846.
40. 'Standard Test Method for Determining Gas Permeability Characteristics of Plastic Film and Sheeting,' *ASTM D1434 – 82*, (Reapproved 2009).

Publications to date:

D. J. Tallman, J. Yang, L. Pan, B. Anasori, M.W. Barsoum. "Reactivity of Zircaloy-4 with Ti_3SiC_2 and Ti_2AlC in the 1100–1300 °C temperature range", J. Nucl. Mater. **460** (2015) 122-129.

G.W. Bentzel, M. Ghidiu, B. Anasori, M.W. Barsoum. "On the Interactions of Ti_2AlC, Ti_3AlC_2, Ti_3SiC_2 and Cr_2AlC with Silicon Carbide and Pyrolytic Carbon at 1300 °C", J. Europ. Ceram. Soc. **35** (2015) 4107-4114.

D. Tallman, E.N. Hoffman, E. Caspi, B. Garcia-Diaz, G. Kohse, R.L. Sindelar, M.W. Barsoum, "Effect of Neutron Irradiation on Select MAX Phases", Acta Mater, **85** (2015) 132–143.

D. Tallman, L. He, E. M. Hoffman, B. Garcia-Diaz, G. Kohse, R.L. Sindelar, M.W. Barsoum, "Effect of Neutron Irradiation on Defect Evolution in Ti_2AlC and Ti_3AlC_2", J. Nucl. Mate., **468** (2016) 194-206.

Number of students/post-docs participating

    a. Grady Bentzel, graduate Ph.D. student, US
    b. Darin J. Tallman, graduate Ph.D. student, US

Appendix A: Figures
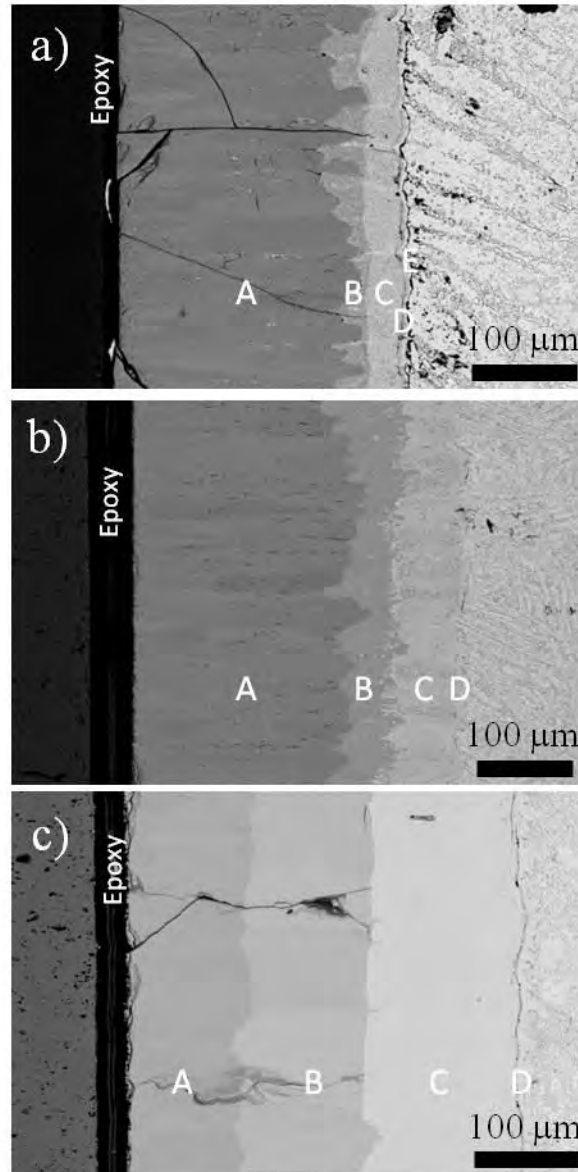
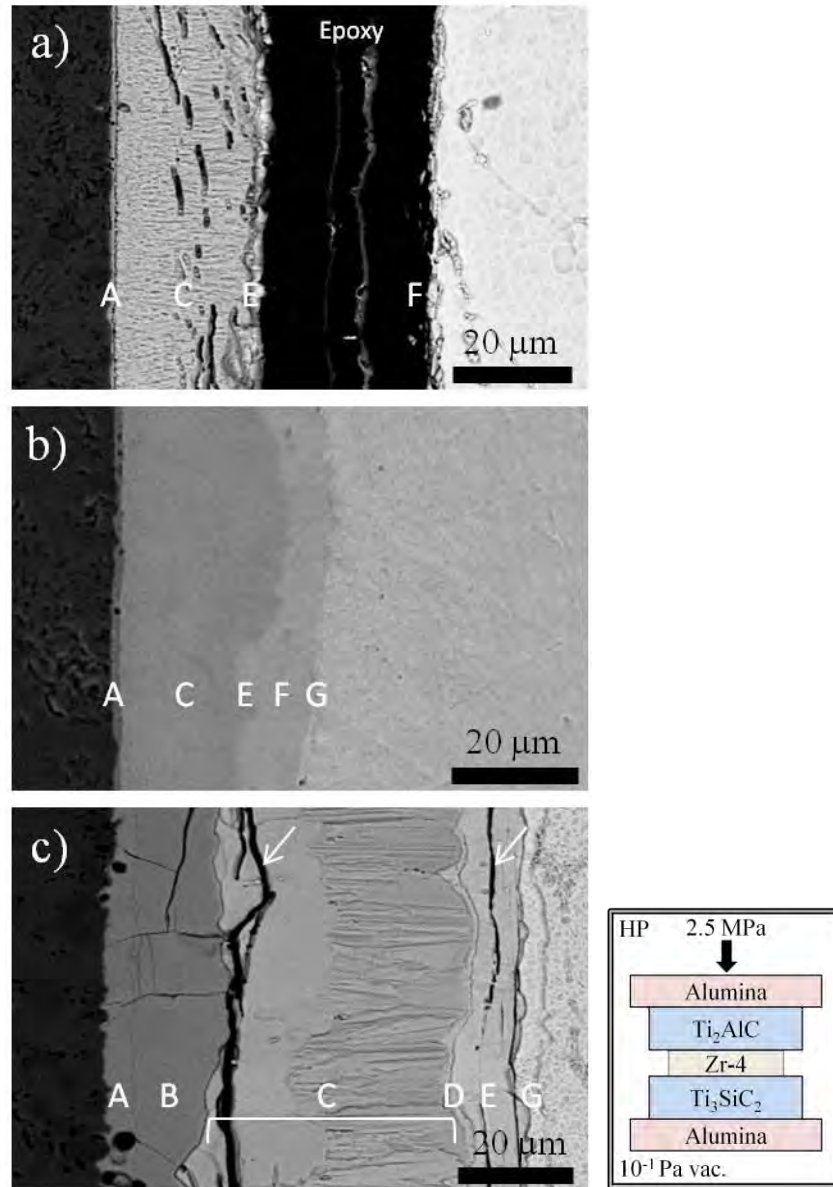**Figure 1. Typical backscattered electron SEM micrographs of Ti$_2$AlC/Zr-4 diffusion couples annealed at a) 1100 °C (etched), b) 1200 °C (etched), and c) 1300 °C for 30 h. The layers A, B, C, D, and E correspond to the phases Zr$_2$Al$_3$, Zr$_5$Al$_4$, Zr$_3$Al$_2$, Zr$_2$Al, and Zr$_3$Al, respectively. In all cases, a layer of epoxy is seen where the diffusion couple fractured during sample mounting. Zr$_3$Al precipitates are observed along the β-Zr grain boundaries beyond the intermetallic layers. At 1300 °C, no single layer dominates. Significant cracking of the intermetallic layers is observed parallel and perpendicular to the original interface.**
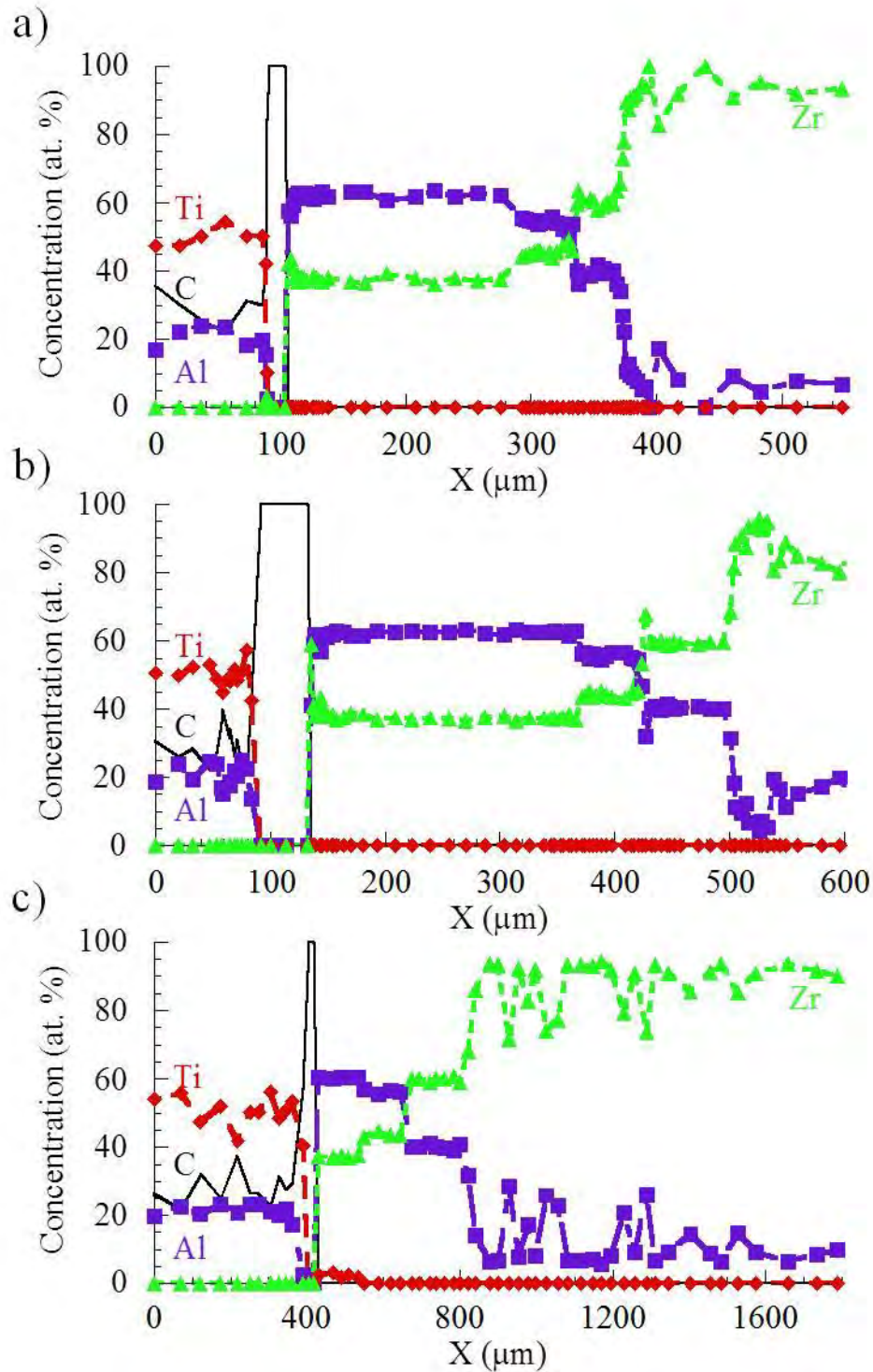
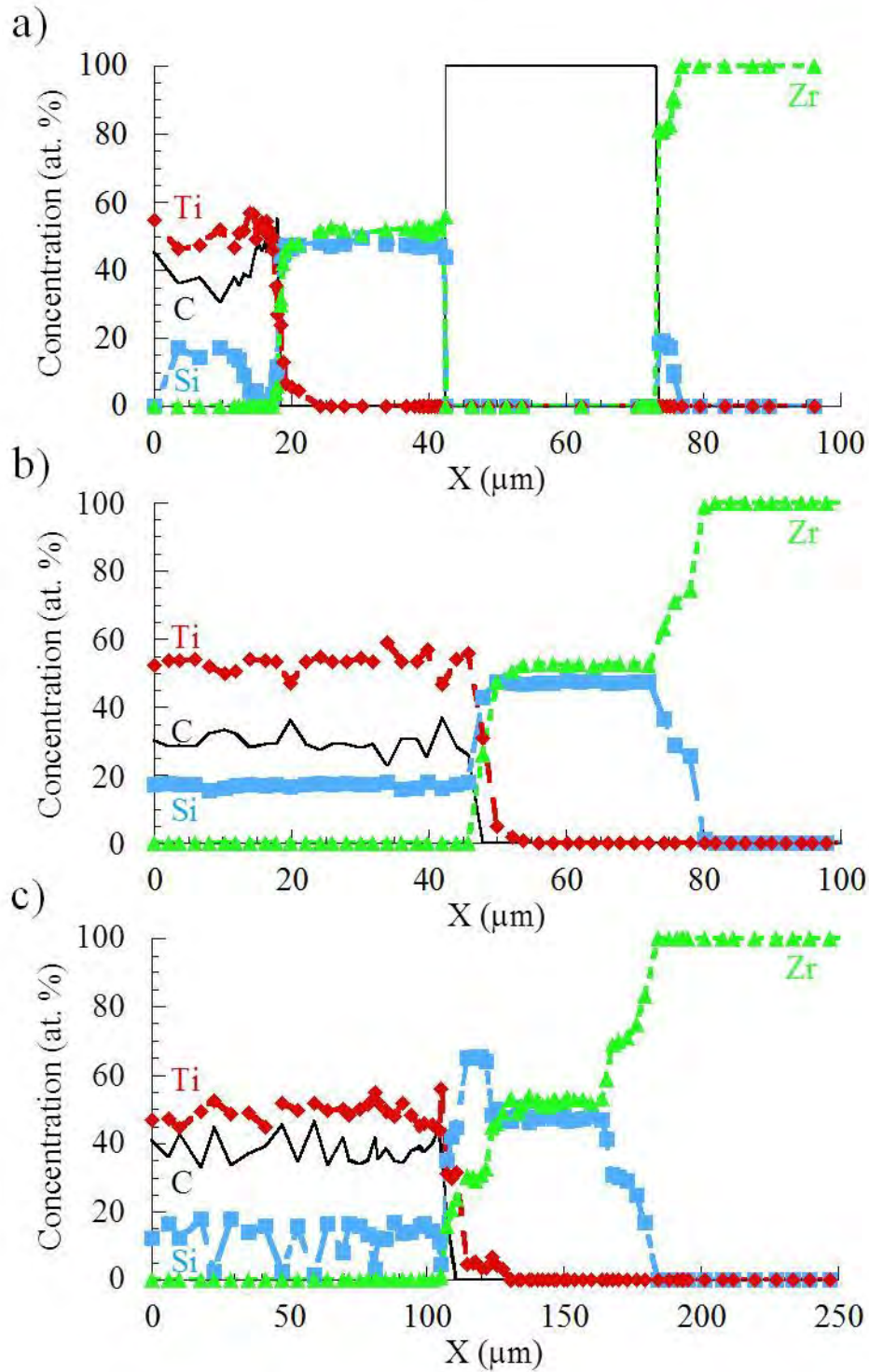**Figure 3. Typical composition profiles of constituent elements determined by EDX line scans normal to the Ti₂AlC/Zr-4 interfaces obtained after annealing at, a) 1100 °C, b) 1200 °C, and c) 1300 °C for 30 h reveal the formation of several intermetallic layers with distinct compositions. Each condition tested resulted in similar phase compositions, with layer thickness increasing with temperature. During annealing at the temperatures tested, the Al dissolves into solution with β-Zr beyond the intermetallic layers on the Zr-4 side. Upon cooling, Al segregation at the grain boundaries likely resulted in the precipitation of Zr₃Al structures, seen in Fig. 1**

23

Figure 3. Typical backscattered electron SEM micrographs of Ti$_3$SiC$_2$/Zr-4 diffusion couples annealed at a) 1100 °C (etched), b) 1200 °C, and c) 1300 °C (etched) for 30 h. The layers A, B, C, D, E, F, and G correspond to the phases (Zr,Ti)Si, ZrSi$_2$, ZrSi, Zr$_3$Si$_2$, Zr$_2$Si, Zr$_3$Si, and β-Zr+Si, respectively. In each case, a thin layer of porosity is observed at the interface. The predominant layer is composed of ZrSi. Occasional cracks, denoted by white arrows, are observed parallel to the interface. Inset of a) shows a schematic of the diffusion couple loading assembly that was in turn placed in the hot press. A layer of epoxy is seen in a) where the diffusion couple fractured during sample mounting.

Figure 4. Typical composition profiles of constituent elements determined by EDX line scans normal to the Ti$_3$SiC$_2$/Zr-4 interfaces obtained after annealing at, a) 1100 °C, b) 1200 °C, and c) 1300 °C for 30 h reveal the formation of several intermetallic layers with distinct compositions. A depletion of Si is seen on the Ti$_3$SiC$_2$ side at 1100 °C (a), though not at higher temperatures. There is a slight counter diffusion of Ti and Zr, though Si is the dominant diffusing species. At 1300 °C, a layer of ZrSi$_2$ is observed.
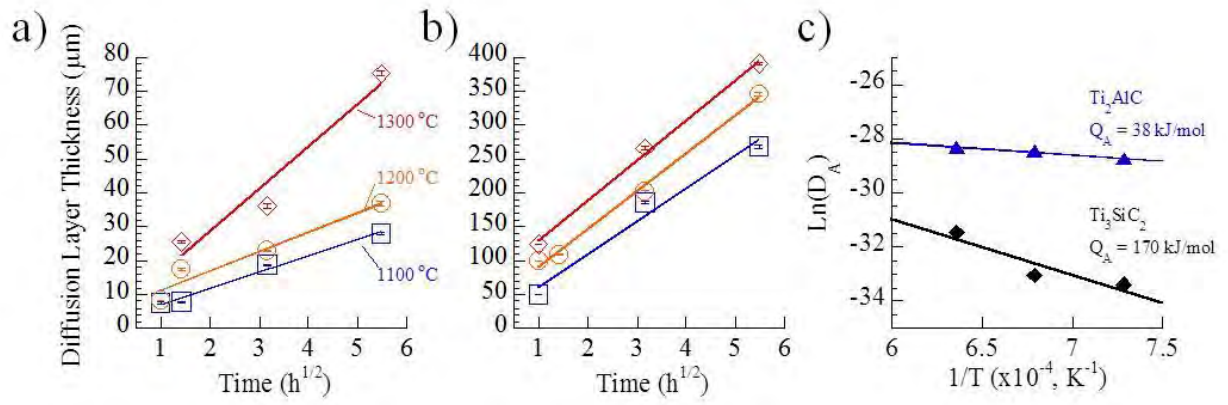
Figure 5. Total diffusion distance (x) vs. $t^{1/2}$ for diffusion couples of: a) Ti_3SiC_2 and, b) Ti_3AlC_2 with Zr-4 in the temperature range of 1100-1300 °C. In all cases, Ti_3SiC_2 results in a shallower diffusion length. These trends show a parabolic diffusion behavior as $x \approx \sqrt{(2Dt)}$. c) Arrhenius plot of the effective diffusion coefficients, D_A.
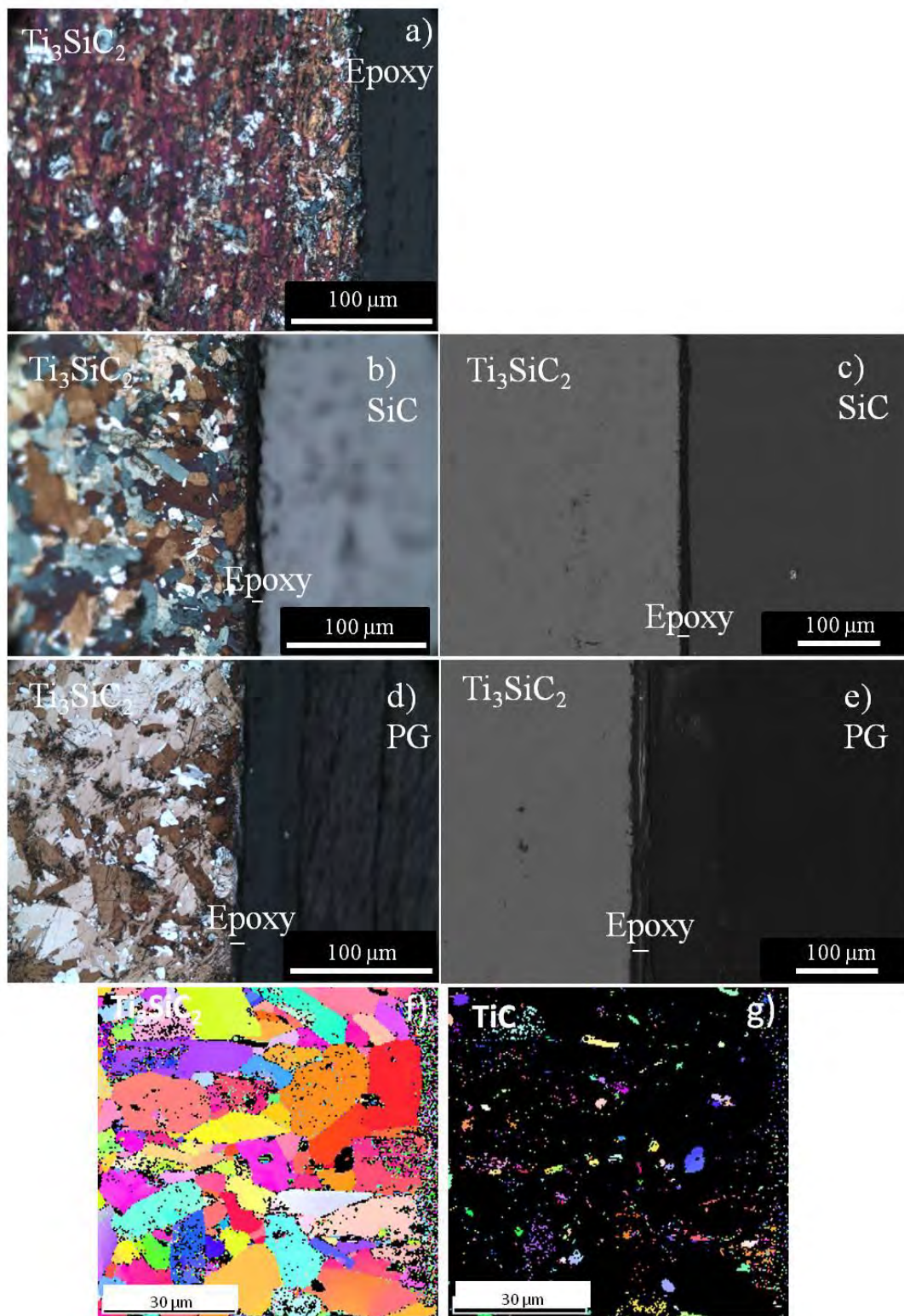
Figure 6: Microstructure Ti$_3$SiC$_2$ after heating to 30 h at 1300 °C in vacuum, a) OM micrographs of cross-sectional polished and etched surface. In contact with SiC for 30 h at 1300 °C, b) OM micrographs of etched surface; c) backscatter electrons SEM micrograph. In contact with PG for 30 h at 1300 °C, d) OM micrograph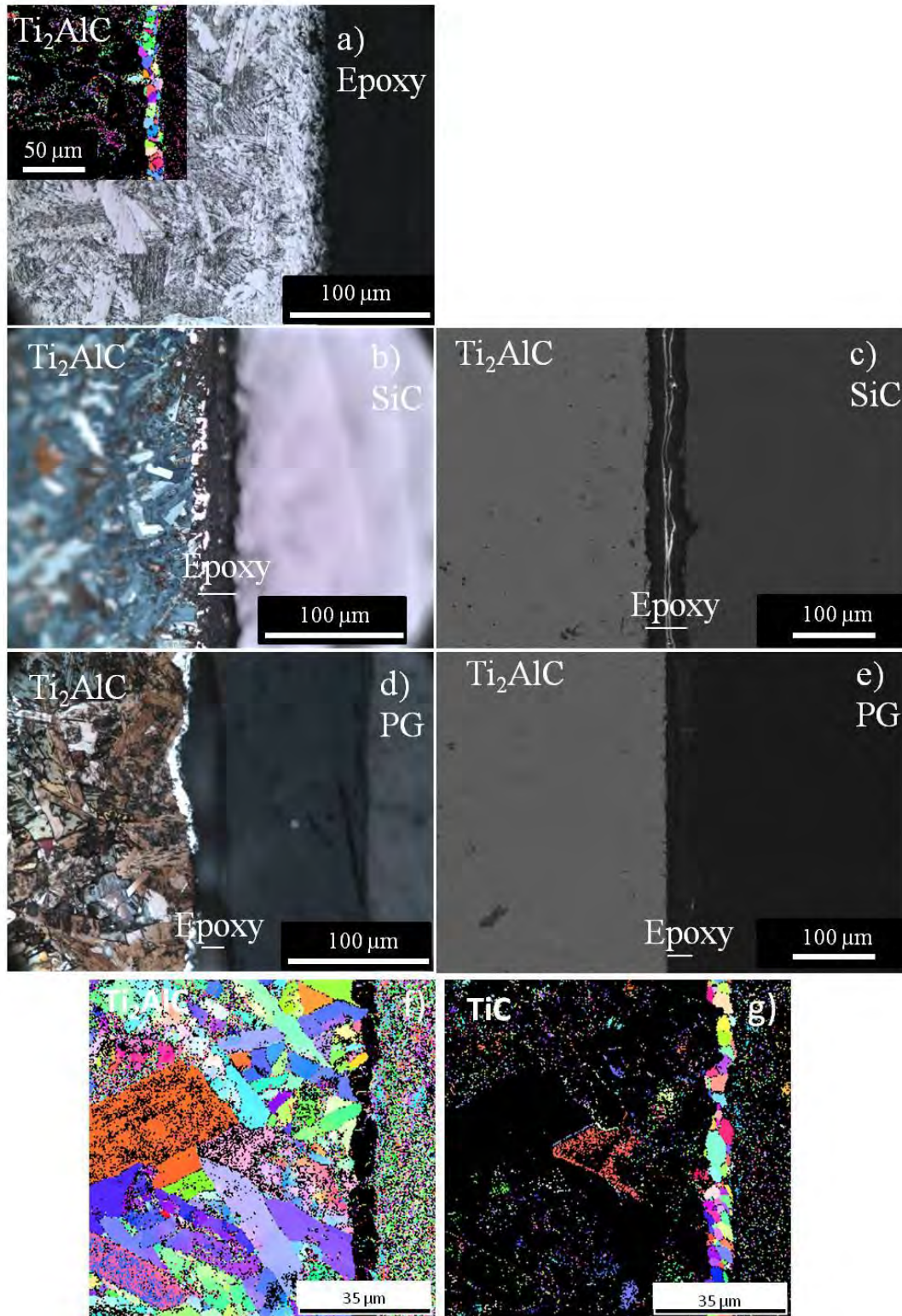s of etched surface; e) backscatter electrons SEM micrograph, EBSD maps of, f) Ti$_3$SiC$_2$ and g) TiC in f. The interface is near the right edge.
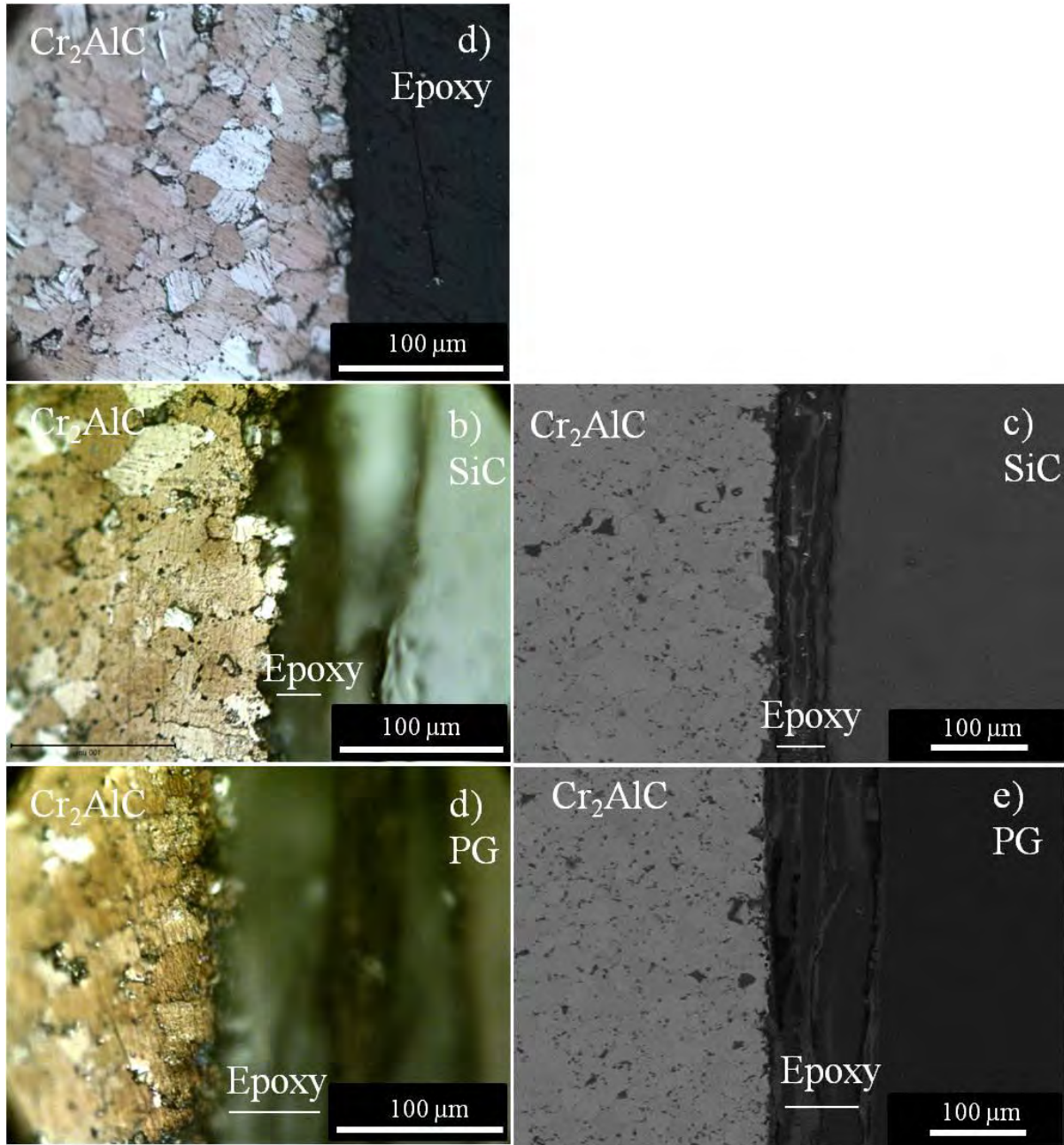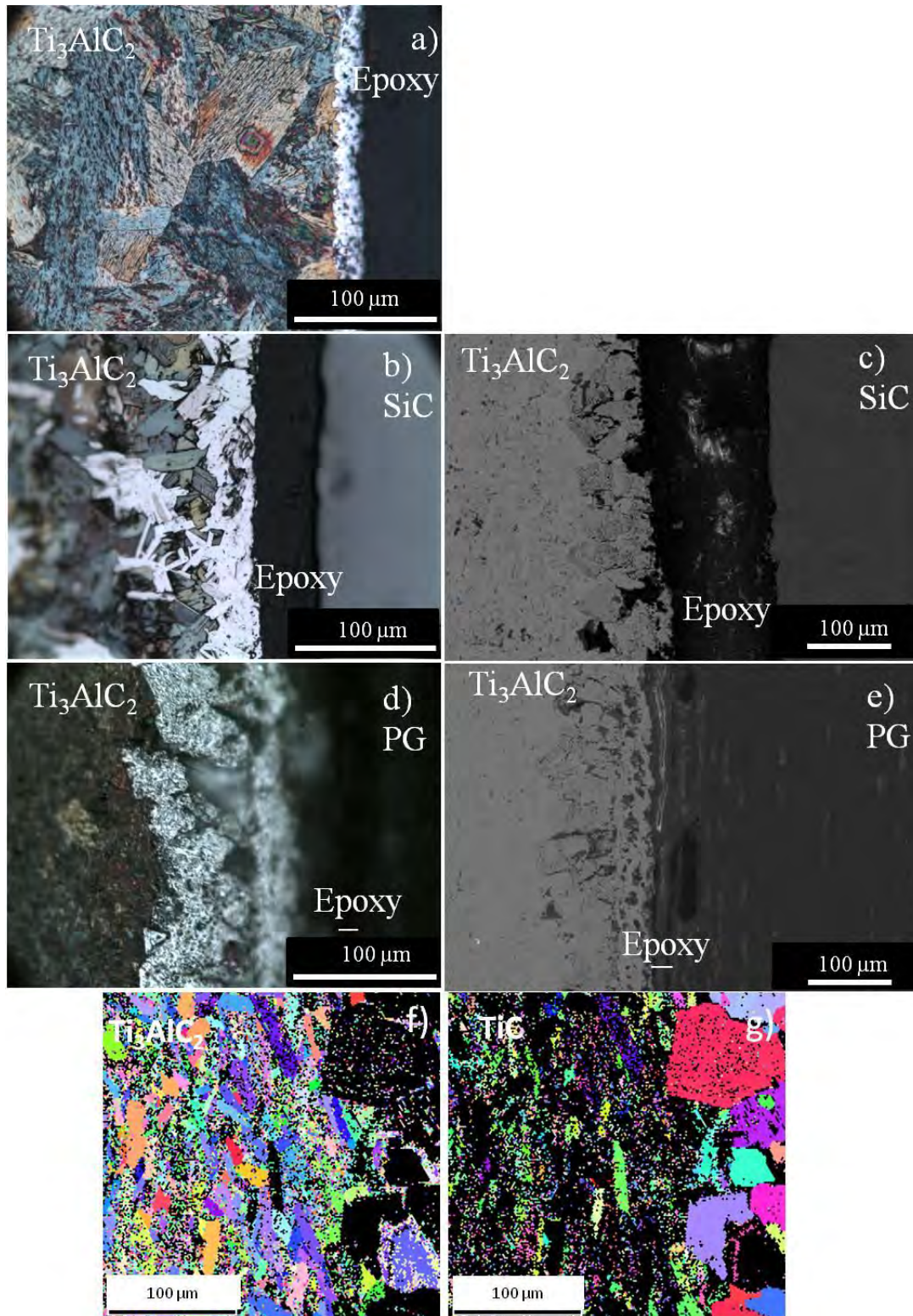
Figure 7: Microstructure Cr₂AlC after heating to 30 h at 1300 °C in vacuum, a) OM micrographs of cross-sectional polished and etched surface. In contact with SiC for 30 h at 1300 °C, b) OM micrographs of etched surface; c) backscatter electrons SEM micrograph. In contact with PG for 30 h at 1300 °C, d) OM micrographs of etched surface; e) backscatter electrons SEM micrograph.

Figure 8: Microstructure Ti₂AlC after heating to 30 h at 1300 °C in vacuum, a) OM micrographs of cross-sectional polished and etched surface. Inset is an EBSD map of TiC confirming the formation of a 10 μm thick TiC layer. In contact with SiC for 30 h at 1300 °C, b) OM micrographs of etched surface; c) backscatter electrons SEM micrograph. In contact with PG for 30 h at 1300 °C, d) OM micrographs of etched surface; e) backscatter electrons SEM micrograph, EBSD maps of, f) Ti₂AlC and g) TiC in f. The interface is near the right edge.

Figure 9: Microstructure Ti₃AlC₂ after heating to 30 h at 1300 °C in vacuum, a) OM micrographs of cross-sectional polished and etched surface. In contact with SiC for 30 h at 1300 °C, b) OM micrographs of etched surface; c) backscatter electrons SEM micrograph. In contact with PG for 30 h at 1300 °C, d) OM micrographs of etched surface; e) backscatter electrons SEM micrograph, EBSD maps of, f) Ti₃AlC₂ and g) TiC in f. The interface is near the right edge.
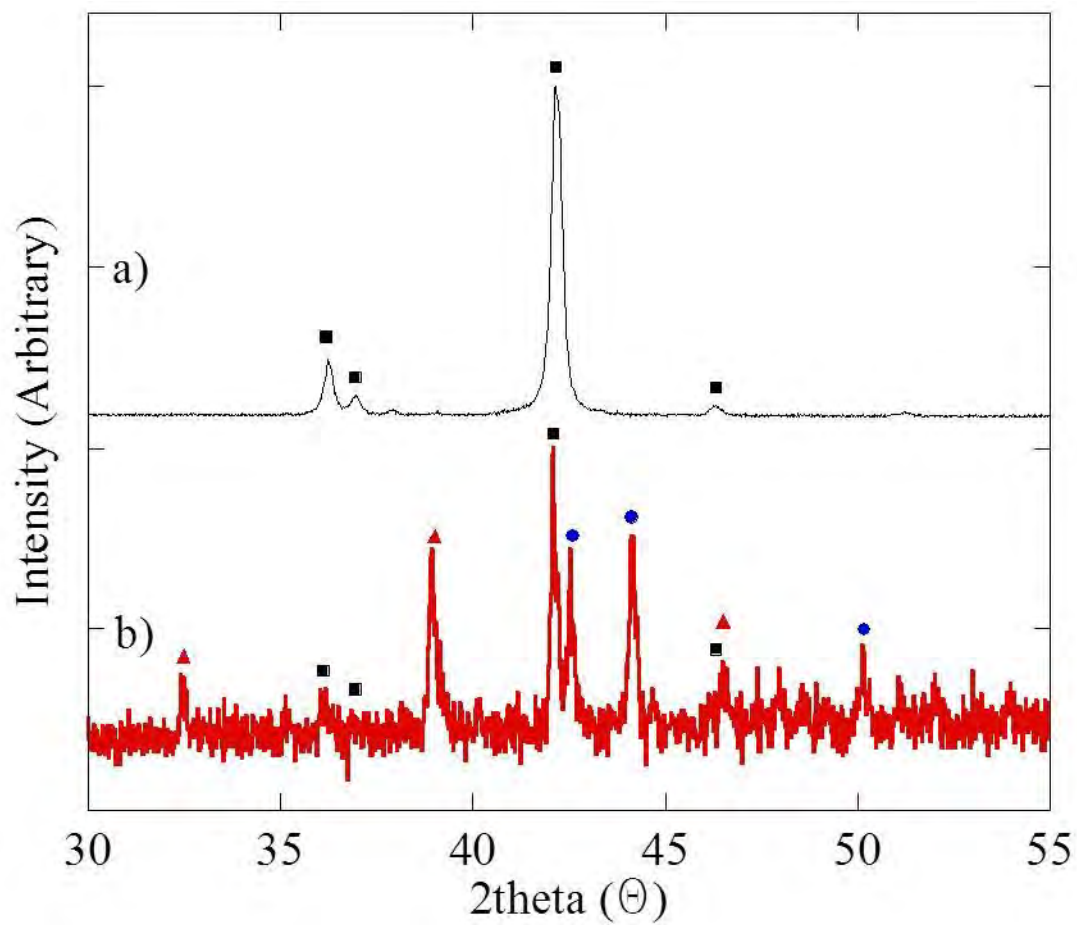
Figure 10: XRD patterns of the surface of, a) unreacted Cr$_2$AlC and, b) Cr$_2$AlC after heating in contact with PG for 30 h at 1300 °C under a load corresponding to a stress of 30 MPa. Black squares represent peak positions of Cr$_2$AlC, blue circles those for Cr$_7$C$_3$, and red triangles those for Cr$_3$C$_2$.
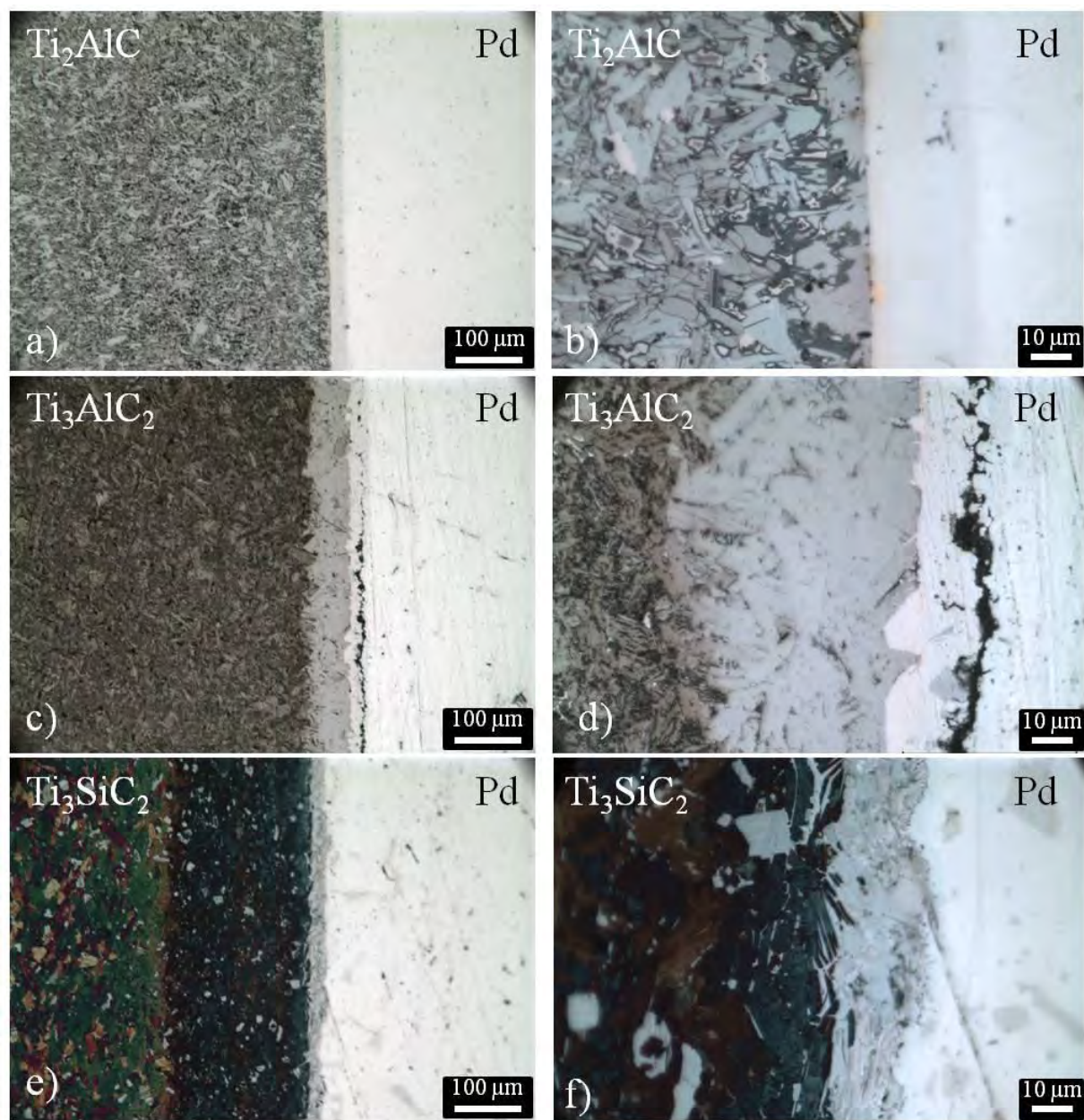
Figure 11: OM micrographs of the etched surfaces of a) and b),Ti$_2$AlC, c) and d), Ti$_3$AlC$_2$, and, e) and f), Ti$_3$SiC$_2$ after interaction with Pd at 900 °C for 2 h.
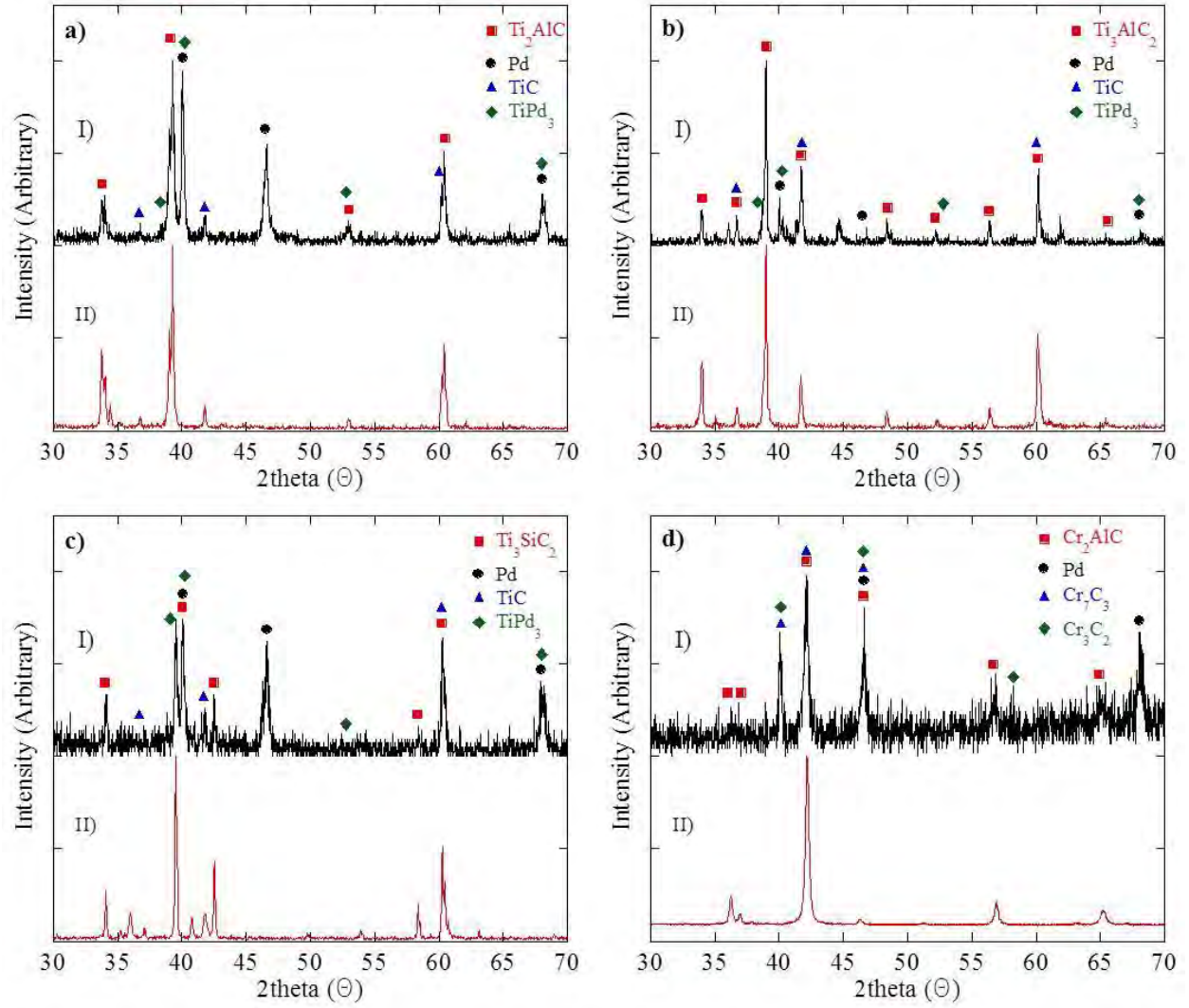
Figure 12: XRD patterns of the interface between , a) Ti₂AlC, b) Ti₃AlC₂, c) Ti₃SiC₂, and d) Cr₂AlC, with, I), Pd after heating at 900 °C for 2 h, and, II), control.

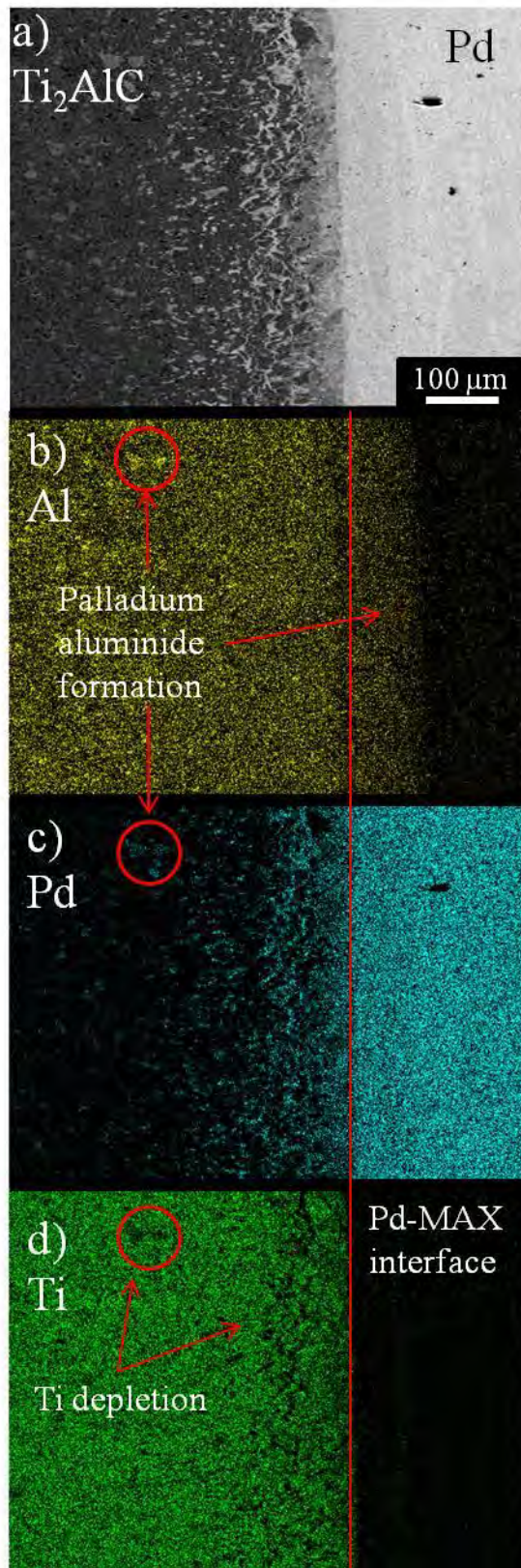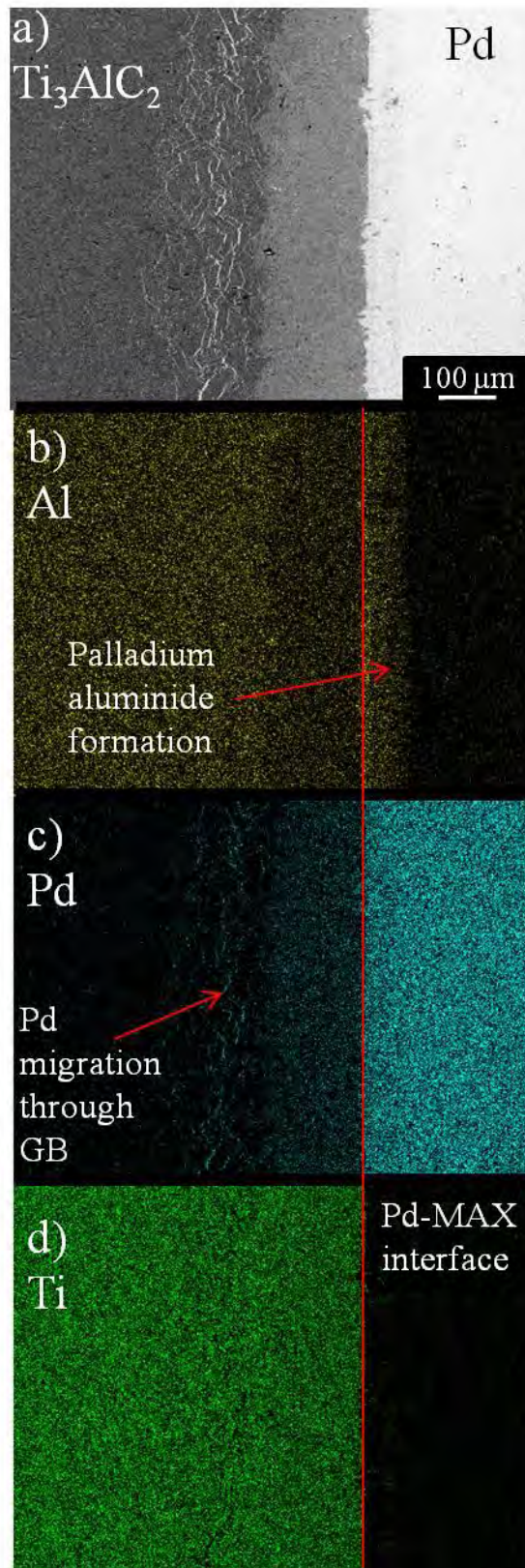**Figure 13: a) Backscatter electron SEM micrographs of the Ti₂AlC/Pd interface after heating to 900 °C 10 h, with elemental mappings of, b) Al, c) Pd, and, d) Ti.**

Figure 14: a) Backscatter electron SEM micrographs of the Ti$_3$AlC$_2$/Pd interface after heating to 900 °C 10 h, with elemental mappings of, b) Al, c) Pd, and, d) Ti.
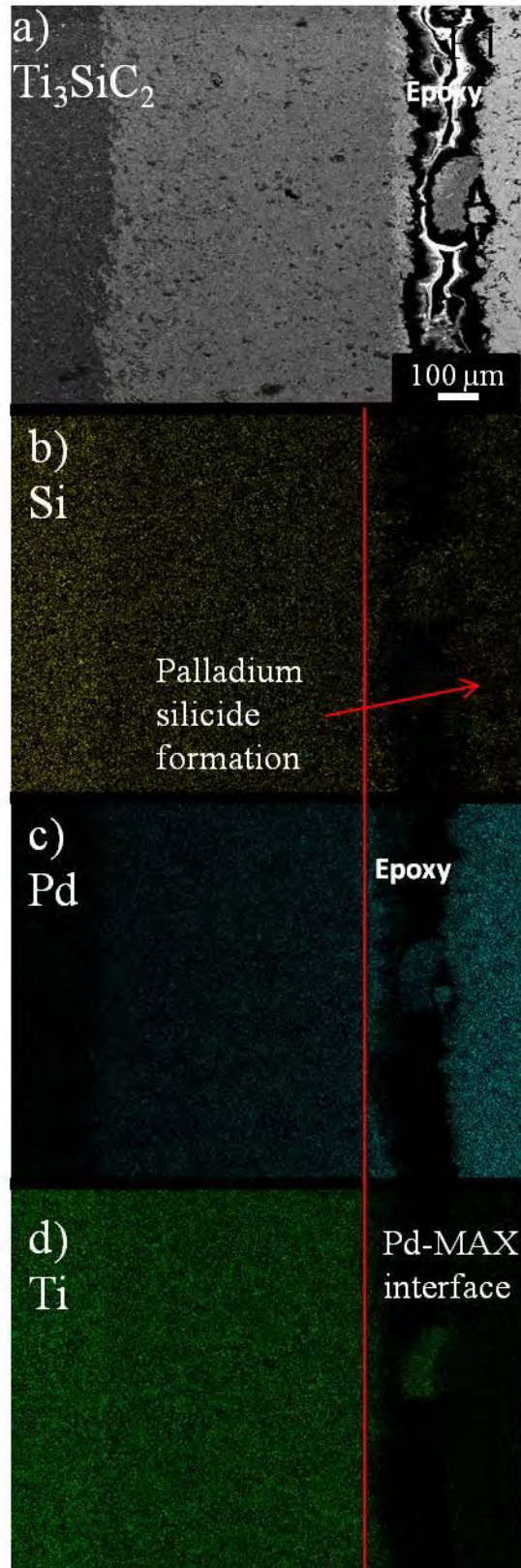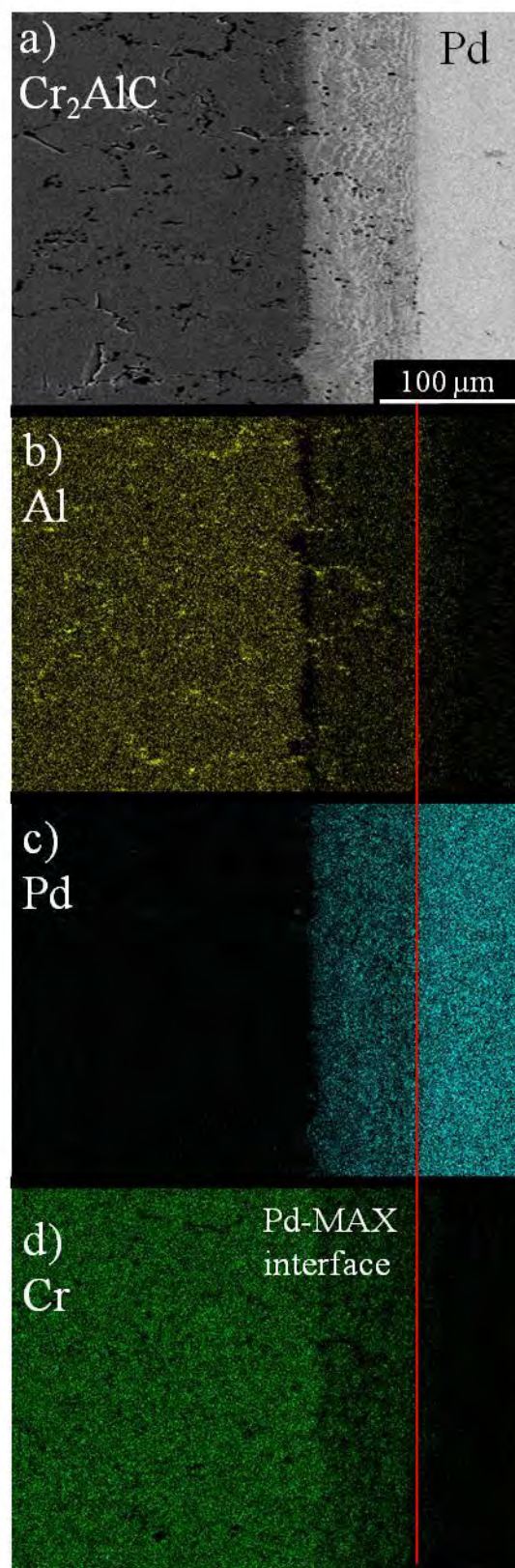
Figure 15: a) Backscatter electron SEM micrographs of the Ti$_3$SiC$_2$/Pd interface after heating to 900 °C 10 h, with elemental mappings of, b) Si, c) Pd, and, d) Ti.

Figure 16: a) Backscatter electron SEM micrographs of the Cr$_2$AlC/Pd interface after heating to 900 °C 10 h, with elemental mappings of, b) Al, c) Pd, and, d) Cr.
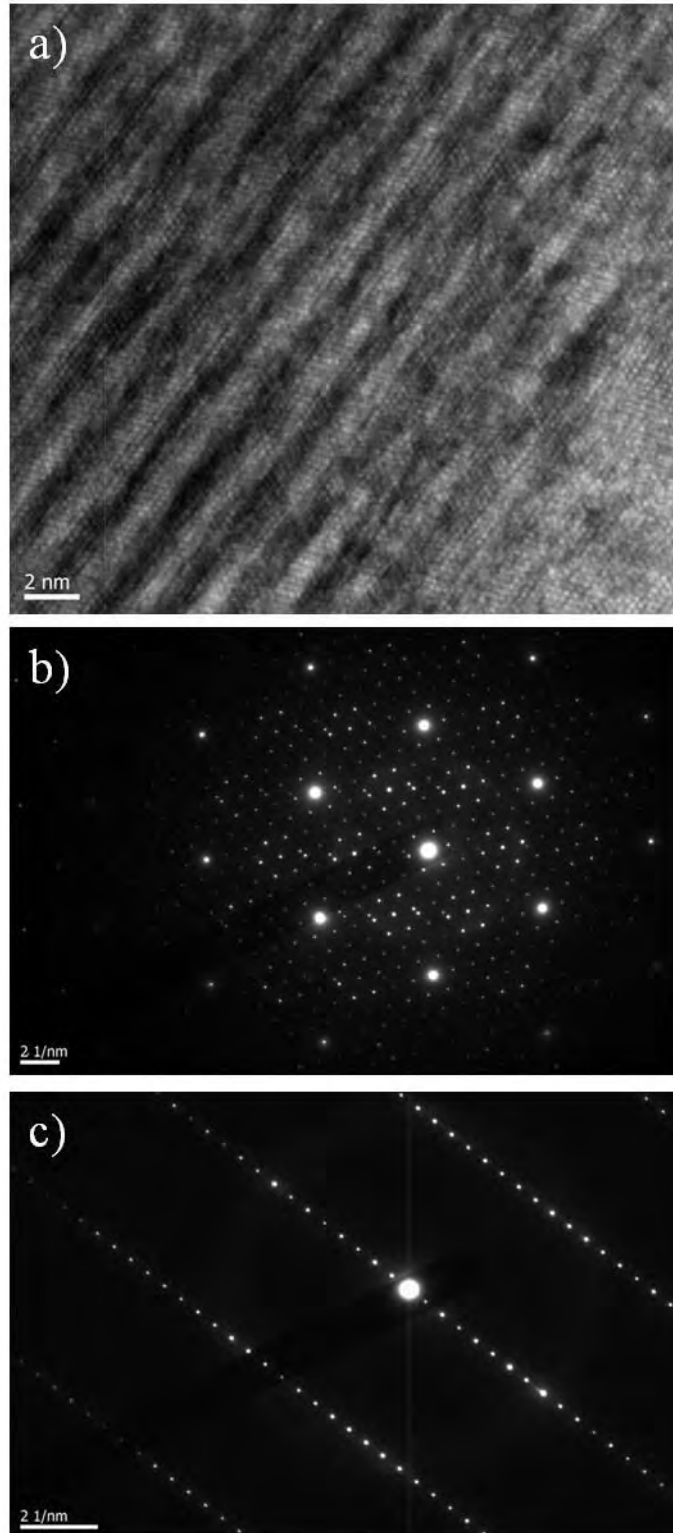
Figure 17: a) HRTEM, and diffraction patterns in the, b) [1121] and, c) [1120] directions of the (Ti,Pd)$_3$SiC$_2$ area from the Ti$_3$SiC$_2$/Pd 900 °C for 2 h sample.
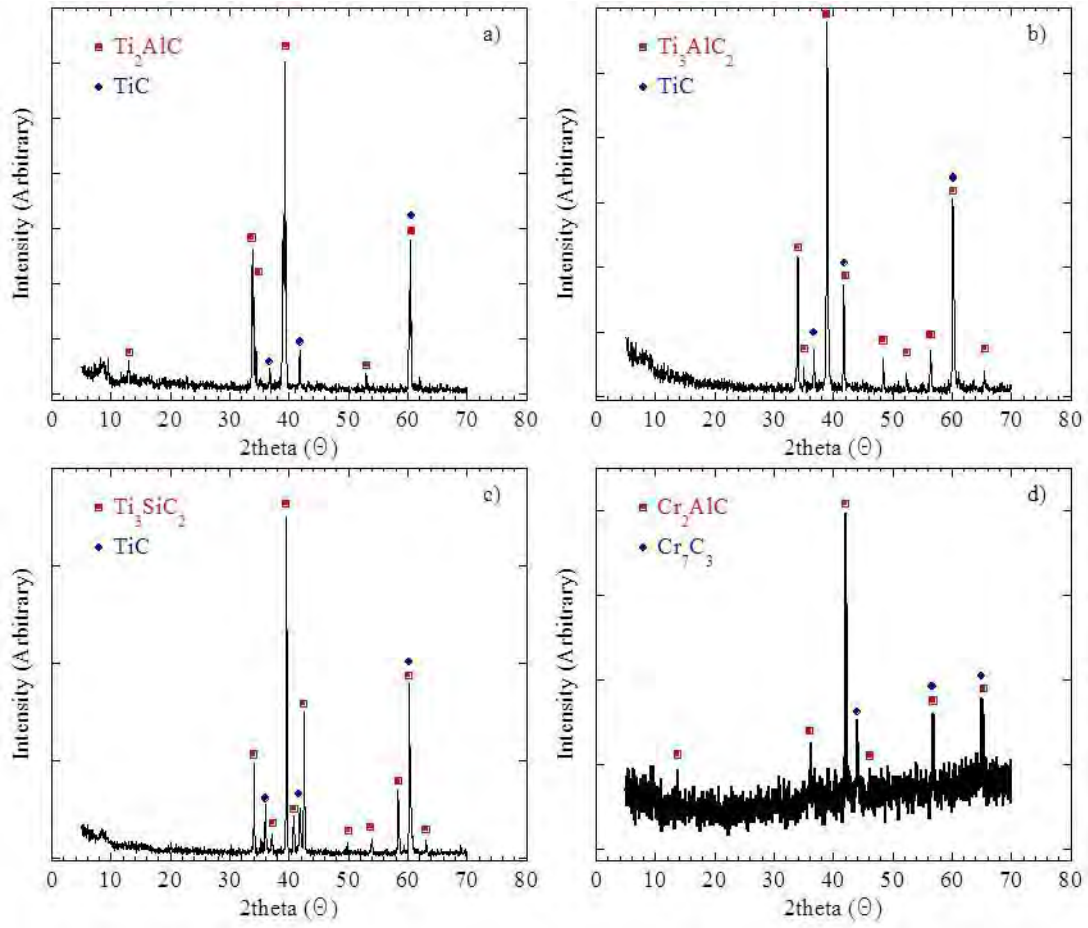
Figure 18: Bulk XRD patterns of surfaces exposed to Na at 750 °C for 168 h of, a) Ti_2AlC, b) Ti_3AlC_2, c) Ti_3SiC_2, and d) Cr_2AlC. Red squares represent the MAX peaks; blue circles represent binary carbide peaks. The latter were the major impurities found in the as-fabricated samples.
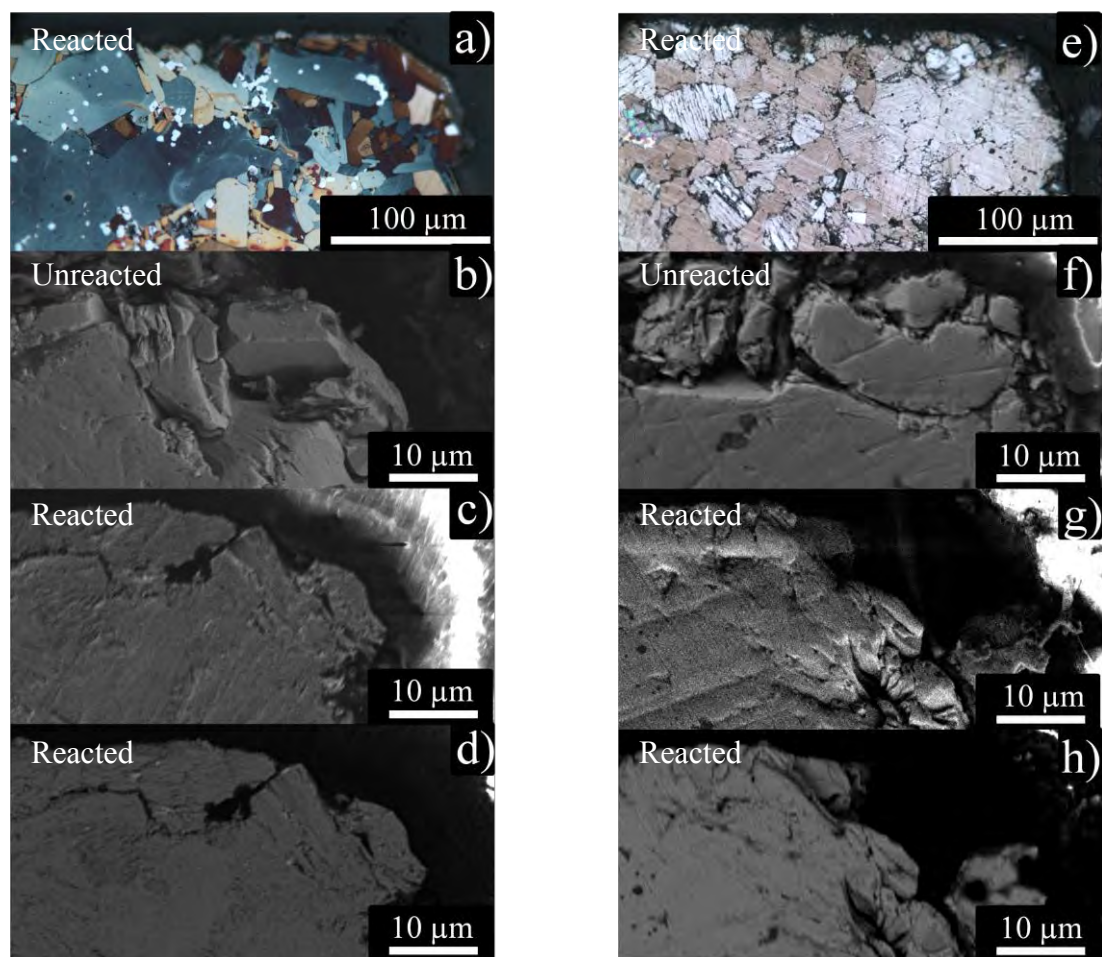
Figure 19: Micrographs of Ti₃SiC₂, Ti_3SiC_2 **a) reacted and etched surface, OM; b) unreacted, SE SEM; c) reacted, SE SEM; d) reacted, BS SEM, and Cr₂AlC,** Cr_2AlC **e) reacted and etched surface, OM; f) unreacted, SE SEM; g) reacted, SE SEM; and, h) reacted, BS SEM, respectively, after contact with Na at 750 °C for 168 h.**
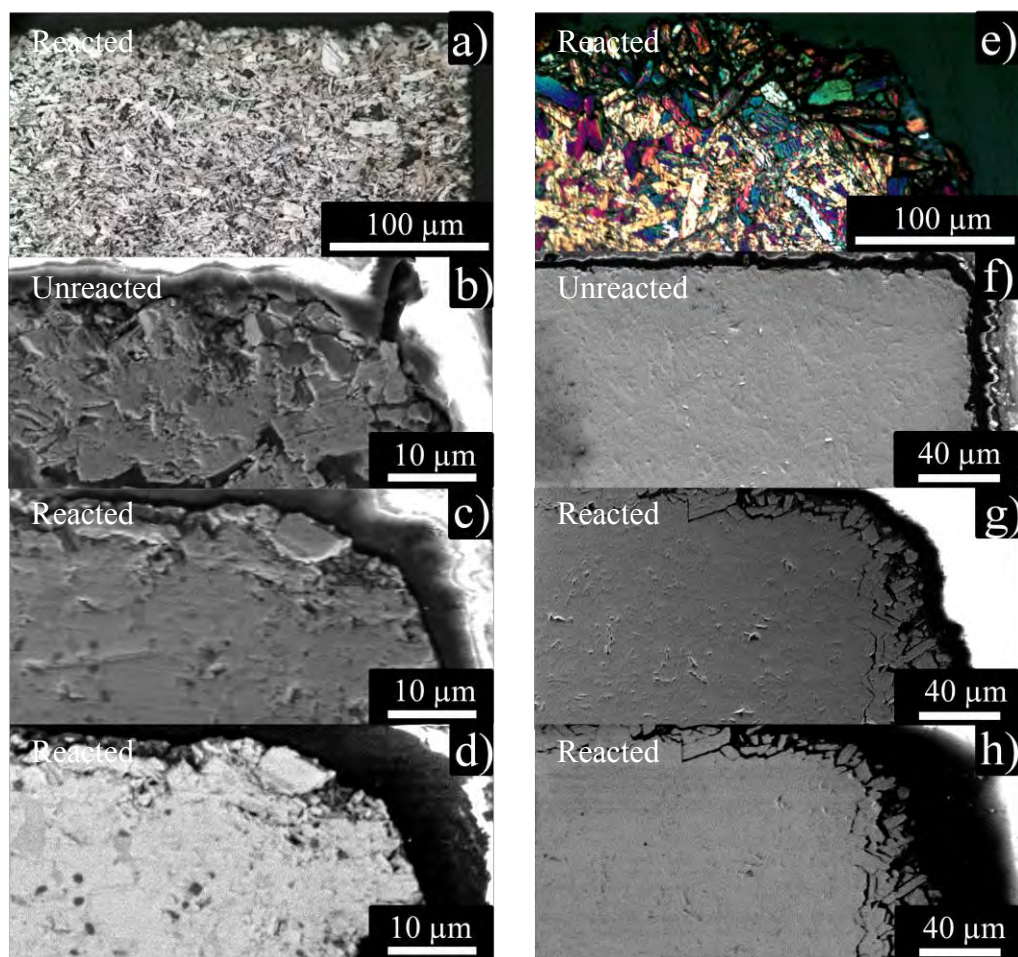
Figure 20: Micrographs of Ti$_2$AlC, a) reacted and etched surface, OM; b) unreacted, SE SEM; c) reacted, SE SEM; d) reacted, BS SEM, and Ti$_3$AlC$_2$ a) reacted and etched surface, OM; b) unreacted, SE SEM; c) reacted, SE SEM; and, d) reacted, BS SEM, respectively, after contact with Na at 750 °C for 168 h.
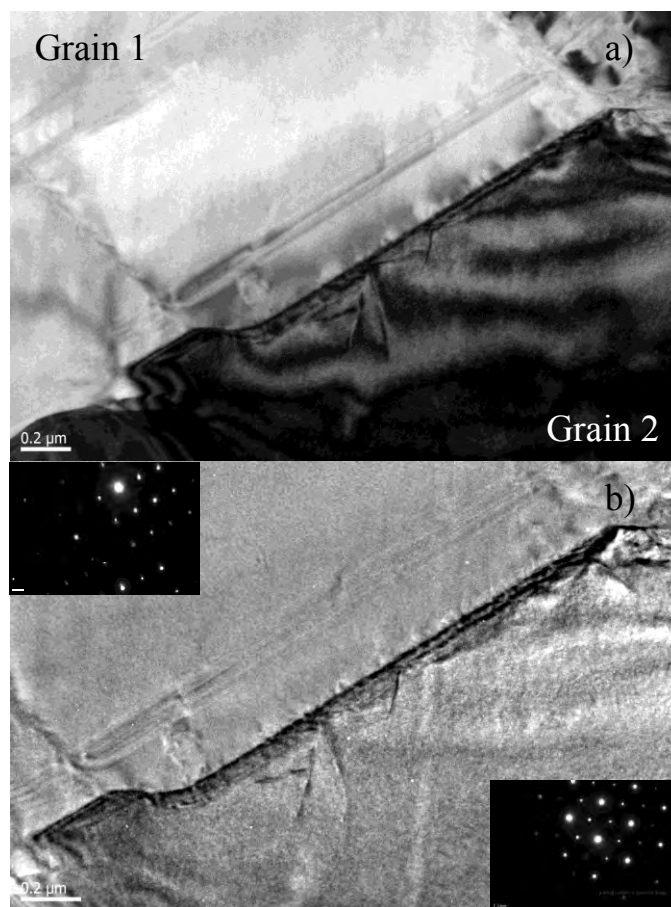
Figure 21: TEM micrographs of Ti₃AlC₂ after contact with Na at 750 °C for 168 h, a) with objective aperture, and, b), normal bright field. Diffraction patterns for grains 1 and 2 are shown as insets.
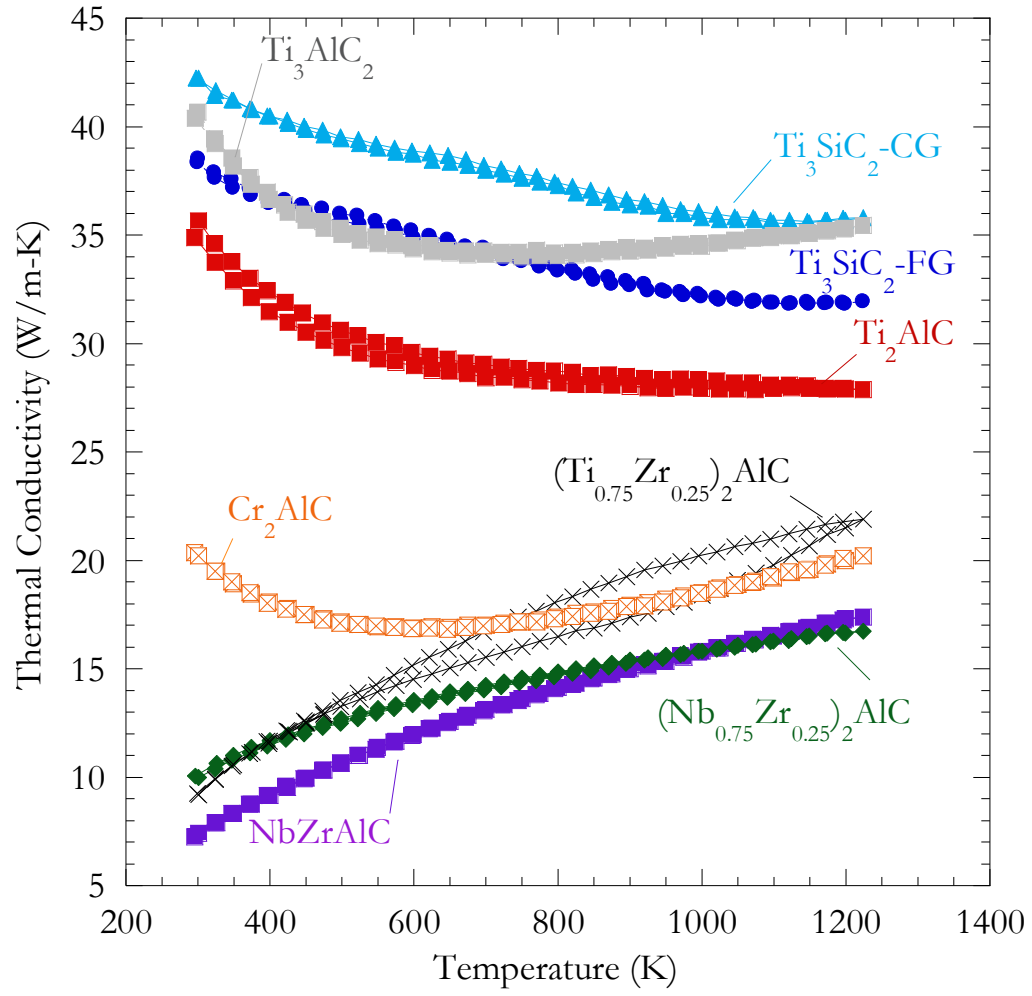
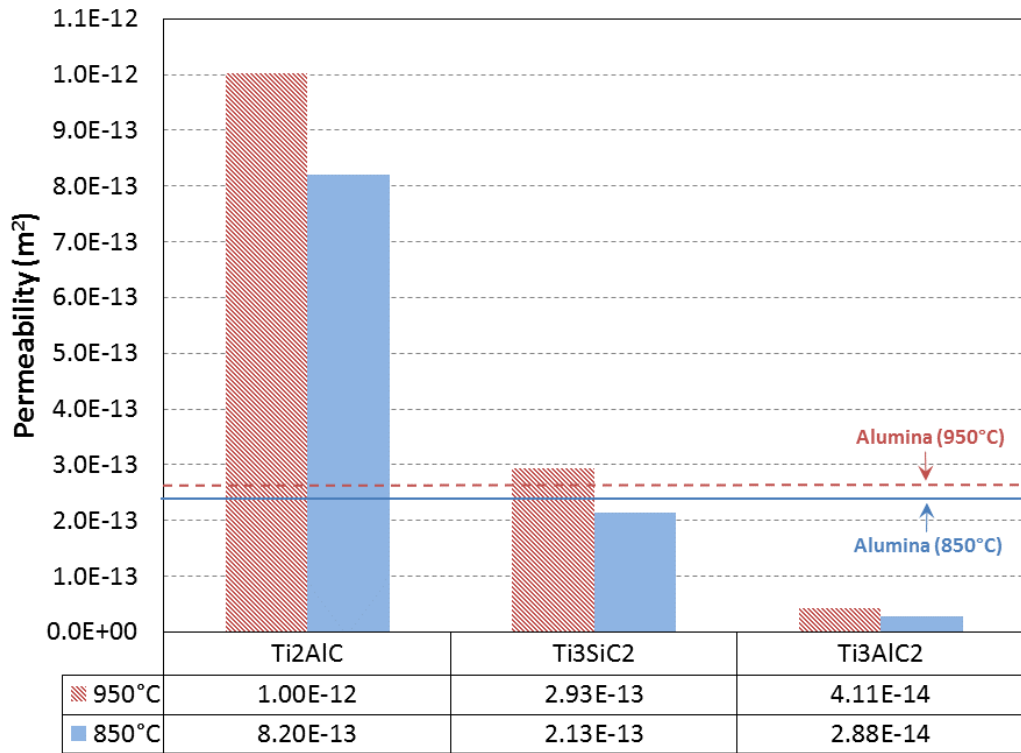**Figure 22: Thermal conductivities of various MAX phases as a function of temperature.**

Figure 23: Permeability coefficient k' of Ti$_2$AlC, Ti$_3$AlC$_2$ and Ti$_3$SiC$_2$ at 850°C and 950°C.

Appendix B: Tables

Table 1: Vickers Hardness values (V_H) at 1 kg force of unreacted cross-section, reacted cross-section, and reacted surface of MAX phases tested herein. Values in parentheses represent one standard deviation.

Vickers Hardness	Ti_3SiC_2	Cr_2AlC	Ti_2AlC	Ti_3AlC_2
Unreacted Cross-section	440(10)	466(8)	458(6)	480(5)
Reacted Cross-section	455(9)	451(5)	467(5)	441(3)
Reacted Surface	450(10)	476(8)	458(2)	399(5)

Table 2 Thermal conductivity κ_{th} of various MAX phases as measured by laser flash analysis.

κ_{th} (W/m-K)	Experimental		Literature		
Sample	300 K	1200 K	300K	1300K	[Ref]
FG-Ti_3SiC_2	38.2	35.9	37	33	[36]
CG-Ti_3SiC_2	39.4	34.1	37	33	[36]
Ti_3AlC_2	39.9	33.8	40	-	[37]
Ti_2AlC	31.6	27.8	46	36	[38]
$(Nb_{0.5}Zr_{0.5})_2AlC$	7.3	17.3	17a	24a	[38]
$(Nb_{0.75}Zr_{0.25})_2AlC$	10.3	17.0	17a	24a	[38]
$(Ti_{0.75}Zr_{0.25})_2AlC$	9.3	21.6	17a	24a	[38]
Cr_2AlC	20.4	20.0	19	16b-	[39]

a- Comparison is made with TiNbAlC, a similar solid solution, as values for these solid solutions are previously unreported.
b- Extrapolated

Table 3 Calculated Thermal κ_e from RT ρ using the Wiedmann-Franz law.[24]

Sample	0.1 dpa, 350 °C			0.1 dpa, 695 °C			0.4 dpa, 350 °C		
	ρ ($\mu\Omega$-m)	κ_e (W/m-K)	κ_{th} (W/m-K)	ρ ($\mu\Omega$-m)	κ_e (W/m-K)	κ_{th} (W/m-K)	ρ ($\mu\Omega$-m)	κ_e (W/m-K)	κ_{th} (W/m-K)
FG-Ti_3SiC_2	1.1(1)	6.8	7.0	0.23(1)	31.3	32.2	1.43(1)	5.1	5.3
CG-Ti_3SiC_2	2.2(1)	3.3	3.4	0.24(1)	30.1	31.1	2.82(1)	2.6	2.7
Ti_3AlC_2	2.84(2)	2.6	4.9	0.39(1)	18.7	36.0	8(2)	.9	1.8
Ti_2AlC	0.75(1)	9.7	22.7	0.44(1)	16.7	38.6	8.3(1)	.9	2.0
Ti_2AlN	1.46(1)	5.0	7.5	0.25(1)	29.7	44.3	3.34(1)	2.2	3.3

Table 4. Permeability of Ti_2AlC, Ti_3AlC_2 and Ti_3SiC_2 at 850°C and 950°C. °C.

Sample	Permeability (K)			
	(mol m)/(m^2 s Pa)		(m^3(STP) m)/(m^2 s Pa)	
	850°C	950°C	850°C	950°C
Ti_2AlC	1.72E-07	1.99E-07	3.87E-09	4.46E-09
Ti_3SiC_2	4.48E-08	5.83E-08	1.00E-09	1.31E-09
Ti_3AlC_2	6.05E-09	8.18E-09	1.36E-10	1.83E-10

Table 5. Equivalent Darcy's permeability coefficient of Ti_2AlC, Ti_3AlC_2 and Ti_3SiC_2 at 850°C and 950°C.

Sample	Equivalent Darcy's Permeability Coefficient (k')	
	m^2	
	850°C	950°C
Ti_2AlC	8.20E-13	1.00E-12
Ti_3SiC_2	2.13E-13	2.93E-13
Ti_3AlC_2	2.88E-14	4.11E-14

Table 6. Permeance of Ti_2AlC, Ti_3AlC_2 and Ti_3SiC_2, with a thickness of 3mm, at 850°C and 950

Sample	Permeance (P)			
	mol/(m^2 s Pa)		m^3(STP)/(m^2 s Pa)	
	850°C	950°C	850°C	950°C
Ti_2AlC	5.75E-05	6.64E-05	1.29E-06	1.49E-06
Ti_3SiC_2	1.49E-05	1.94E-05	3.35E-07	4.36E-07
Ti_3AlC_2	2.02E-06	2.73E-06	4.52E-08	6.11E-08